FINE-GRAINED INORGANIC SEDIMENT CHARACTERISTICS AND SIZE DISTRIBUTION FROM THE LAST 30 KY IN THE EASTERN EQUATORIAL PACIFIC AS COMPOSITIONAL AND CURRENT INTENSITY PROXIES

Paul Robert Auerbach

SUBMITTED IN PARTIAL FULFILLMENT OF THE
REQUIREMENTS FOR THE DEGREE OF COMBINED
HONOURS BACHELOR OF SCIENCE IN EARTH SCIENCES AND
OCEANOGRAPHY AT DALHOUSIE UNIVERSITY,
HALIFAX, NOVA SCOTIA
MARCH 2006

Dalhousie University

Department of Earth Sciences
Halifax, Nova Scotia
Canada B3H 3J5
(902) 494-2358
FAX (902) 494-6889

DATE: March 13/06

AUTHOR: Paul Robert Auerbach

TITLE: Fine-grained Sediment Characteristics and Size Distribution from the last 30 kY IN The Eastern Equatorial Pacific As Compositional And Current Intensity Proxies

Degree: B.Sc Honours Convocation: May Year: 2007

Permission is herewith granted to Dalhousie University to circulate and to have copied for non-commercial purposes, at its discretion, the above title upon the request of individuals or institutions.

[redacted]
Signature of Author

THE AUTHOR RESERVES OTHER PUBLICATION RIGHTS, AND NEITHER THE THESIS NOR EXTENSIVE EXTRACTS FROM IT MAY BE PRINTED OR OTHERWISE REPRODUCED WITHOUT THE AUTHOR'S WRITTEN PERMISSION.

THE AUTHOR ATTESTS THAT PERMISSION HAS BEEN OBTAINED FOR THE USE OF ANY COPYRIGHTED MATERIAL APPEARING IN THIS THESIS (OTHER THAN BRIEF EXCERPTS REQUIRING ONLY PROPER ACKNOWLEDGEMENT IN SCHOLARLY WRITING) AND THAT ALL SUCH USE IS CLEARLY ACKNOWLEDGED.

Abstract

The nature of deep-sea sediments is important for understanding the mechanisms of sediment delivery and deposition to the deep ocean. This study describes and analyzes the size distribution of fine-grained biogenic opal and inorganic bottom sediments in the biologically productive, active upwelling region of the Eastern Equatorial Pacific (EEP). Using the Coulter Multisizer II, samples of biogeneous silica, inorganic silt and clay grains are analyzed from various depths in the seabed through a 200cm cored interval that spans the age range of 1-30 ky B.P. Downcore variation in grain sizes is inferred to record changes in regional paleocurrent variability as well as fine siliclastic and opal delivery to the site. Results show that biogenic silica, in the form of opal, coarsens the sediments. However, this effect is not exhibited in the Holocene. Decreased delivery of mineral aerosols is inferred to be a mechanism to enhance the fine grain fraction of the samples. In agreement with other studies, stable paleocurrents are thought to characterize the 15 – 30 ky B.P period. Comparatively, the 1 – 15 ky B.P interval shows a more variable flow regime and is attributed to short-term instabilities of deep-water masses. For the paleocurrent reconstruction over latter interval, an anti-correlation is observed with respect to deep-water currents in the North Atlantic suggesting a dynamic inter-play between the Atlantic and Pacific deep water masses in global ocean thermohaline circulation in the Late Quaternary.

Key Words: grain size, paleocurrent intensity, biogenic opal, Eastern Equatorial Pacific

ACKNOWLEDGEMENTS

Much thanks goes out to my family and friends who were always there to offer kind words of support and encouragement. I would also like to express my utmost appreciation for the patience, insight and dedication exhibited by my two advisors, Paul Hill and Markus Kienast. Thank you so much for teaching me how to conduct good scientific research as well as showing me the great importance of one's imagination in understanding the many processes in oceanography and geology. My gratitude must go out to Kristian Curran who has become, and will continue to be, a great role model for me. Thank you so much for the vast generosity you displayed while helping to facilitate my undergrad thesis and I certainly could not have done it without you. I wish Kristian, his wife, and his soon-to-be new addition to the family only good health and utmost joy in the future.

Table of Contents

Table of Figures

CHAPTER 1: INTRODUCTION

1.1 Background

The environmental record preserved in deep-sea sediments offers valuable insight into the dynamic inter-play of earth processes, especially when considering the dynamics occurring within the water column (Futterer 2000). Of increasing interest in studies of deep-sea sediments is the reconstruction of high-resolution cycles of climatic change for recent glacial-interglacial periods (Hall and McCave 2000; Sigman and Boyle 2000). Various methods have been proposed to resolve high-frequency events in the late Quaternary deep-sea sediment record (Bacon 1984; Hall and McCave 2000; Loubere et al. 2004), such as changes in the export of particulate matter out of the water column into bottom sediments and changes in the movement of deep water masses .

Numerous authors have suggested that variations exist in sedimentation dynamics during inter-glacial and glacial periods (Bacon 1984; Bianchi and McCave 1999; Loubere et al. 2004). A central premise of these studies is that there are measurable differences in both material flux and style of sedimentation for these periods. Changes in sedimentation, in particular, changes in the flux of sediments reaching the sea floor, have been inferred using sediment textural parameters in conjunction with isotopic proxies (Hall and McCave 2000, Kienast et al. 2005, *submitted*).

The nature and rates of sedimentation in the Eastern Equatorial Pacific (EEP) have been of particular interest because it is a zone of oceanic upwelling with high levels of primary production (Mix et al. 2003). This region lies close to a boundary where seafloor sediments are dominated by either diatomaceous or calcareous ooze (Seibold and Berger 1993), so zonal shifts in water column processes can be resolved in the sediment record. In attempts to characterize the rates of pelagic sedimentation for the study site for the last 30 ky (ky = thousand years), however, discrepancies have arisen when comparing mass accumulation rates (MAR) and Thorium-230-based particle flux measurements. The inferred MAR suggests 50-100 percent more sediment accumulation than the estimate derived from Thorium-230 proxy over the core interval examined in this study (Kienast et al. 2005, submitted manuscript). One mechanism put forth to explain these inconsistencies in sedimentation rate involves a component of horizontal or lateral advection of particulate material as a result of variability in bottom water currents (Kienast et al. 2005, submitted manuscript; Zabel et al. 2000). The goal of this study is to examine sediment textural changes over a section of core from the EEP that spans the last 30 k.y. The textural changes will be used to infer changes in sedimentation and to comment on the debate regarding sedimentation rates in the EEP.

CHAPTER 2: SAMPLE PREPARATION METHODS AND PARAMETERIZATIONS

2.1 Core Selection

Core ME-0005-27JC was obtained from the Eastern Equatorial Pacific at a longitude of 82°47.20'W and latitude of 1°51.201'S (Fig. 2.1). This core was extracted from the sea floor at a water depth of 2203 m within the southern lower slope area of the aseismic NE-SW striking Carnegie Ridge separating the Panama and Peru Basins. The locale is of importance for certain facets of paleoceanographic research because it is a known zone of Neogene nutrient upwelling and the seabed contains ash layers related to Andean volcanism (Mix et al. 2003). The latter are useful for establishing age control in the core. For this study, the core was sampled from depths of 4 cm to 197 cm, correlating to an age interval from approximately 1 ky B.P to 30 ky B.P based on carbon-14 age determinations[1].

Core Me-0005-27JC was chosen for this study for two reasons. Firstly, grinding of samples is often part of the sample preparation for chemical analysis and, as such, may not preserve their original size distribution. However, unground samples were available for a textural study of the core. Secondly, it is located in an area where there is considerable debate as to the rate of pelagic sedimentation over the last 30 ky.

Interbedded clayey diatom and nannofossil oozes are the predominant lithologies to a depth of approximately 400 m below the seafloor, with minor constituents of silicoflagellates, pyrite, clay and siliclastics (Mix et al. 2003). Bioturbation and mottling were observed throughout the core, and are inferred to represent high biological surface

---

[1] From unpublished data set compiled by Kienast, S.S., Kienast,.M., Francois, R., Mix, A.C., Mollenhhauer G., Eglington, T.I., and S.E. Calvert (2005, *submitted manuscript*)

production and high activity of benthic organisms, respectively (Mix et al. 2003). Seismic reflection, side scan sonar, and textural analyses reveal no evidence of sediment slumping, turbidites or other mass transport processes but, rather, reveal various erosive features: (1) Large abyssal foraminiferal sand dunes and barchans (Seibold and Berger 1993; Londsdale and Malfait 1974), (2) steep, sediment starved ridge flanks indicative of down-slope sediment transport (Mix et al. 2003), and (3) fining of sediment with increasing water depth in the ridge area (Moore et al. 1973).

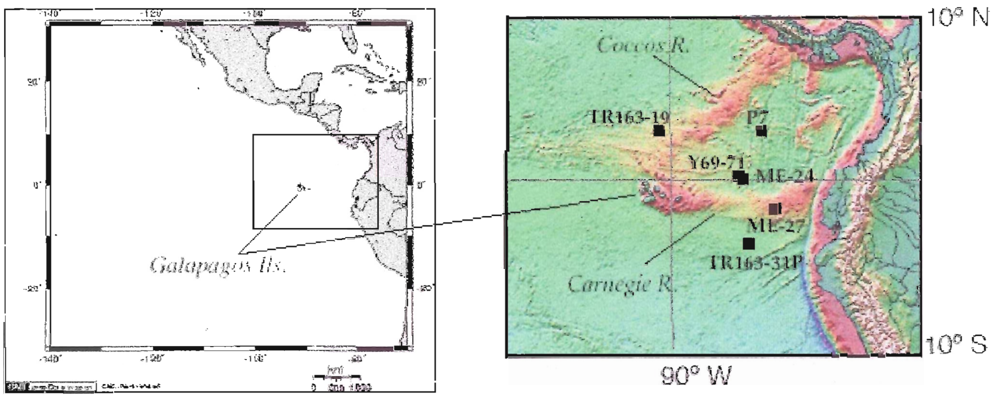

Figure 2.1. Map of Study Area and Core Sites (Modified by Kienast et al. (2005, submitted) after Smith and Sandwell 1997). Note, left-hand figure is an enlargement of the study area (right). This study examines the sediment textures over a 30 k.y interval of core ME-27.

Samples used for this study were extracted normal to bedding. The sub-samples were freeze dried with the aim of removing as much moisture as possible. They were then stored in 25 ml vials labelled with their depth locations in the core. The sediments contain on average 50 % calcite, 39 % siliclastic grains, 10 % biogenic silica, and 1 % organic carbon, by weight[2].

---

[2] From unpublished data set compiled by Kienast, S.S., Kienast,.M., Francois, R., Mix, A.C., Mollenhhauer G., Eglington, T.I., and S.E. Calvert (2005, *submitted manuscript*)

2.2 Sample Preparation

The primary objective of the sample preparation procedure, described in the following sections, was to yield a sample of the sediment material that would allow the Coulter Multisizer II, an electroresistence particle size analyzer, to count and obtain accurate grain-size distributions. More specifically, it was important to ensure that the sample did not contain organic material and calcite and that it was disaggregated, so individual mineral grains could be sized and counted. The extent of calcite grain dissolution and diagenesis could not be accounted for and, thus, was removed to enhance control on the chemical composition of samples.

This study followed the sample preparation methods laid out in Milligan and Kranck (1991). The samples were treated with acid and hydrogen peroxide, from now on referred to as "acid digestion", to eliminate calcite and organic carbon. Size analysis was focused, therefore, on the siliclastic and biogenic silica components of the sediment. The process of acid digestion employed for this study started with the extraction of approximately 60 mg ±20 mg of sediment from each jar. A digestive liquid agent of 1 Molar (M) Hydrochloric Acid (HCl) was then prepared for use in treating the sediment samples. This was accomplished by diluting 10 ml of 36 % HCl solution with 100 ml of distilled water. Each sample was treated with 15 ml of the 1M HCl solution in order to dissolve all the calcite in the samples. Once dissolution was complete, the individual jars were heated to 55°C in order to evaporate the HCl from the sample. The dessicated samples were covered with Parafilm® to prevent contamination from dust.

Hydrogen peroxide (H_2O_2) was used to eliminate any organic matter remaining in the samples. Each sample was treated three times with 5 ml, for a total of 15 ml, of 30 %

hydrogen peroxide solution over a 55°C heat source. Similar to the HCl digestion process, the samples were left to dry and subsequently covered with a seal.

The procedure for sample preparation prior to measurement and analysis involved numerous dilutions in a 3 % $NaPO_3$ electrolyte solution. Dilution was required to maintain appropriate concentrations for accurate measurements by the Coulter Multsizer. Initially, 10 ml ± 3 ml of electrolyte solution was added to the acid-digested sample contained in a small 25 ml beaker. The sample was placed in a sonification bath (discussed in following section) to ensure that grains did not remain stuck to the walls of the beaker as a result of the drying process after digestion. The sample was then placed in a larger 250 ml beaker where it was further diluted with 200 ml ± 20 ml of electrolyte solution. The sample containing suspended particles was subsequently passed through a mesh filter to establish an upper limit in grain size appropriate for the Coulter Multisizer II. Using a 25 ml pipette, 10 ml ± 3 ml were extracted from the filtered sample and diluted once more with 120 ml ± 20 ml of the electrolyte solution.

Finally, the sample was sonified for 3 minutes using a sapphire-tipped ultrasonic probe. This last step was used in order to separate the very fine grains that are potentially bound in clusters by weak electrostatic forces. By treating the sample in an ultrasonic bath and sonifier, prior to using the Coulter Multisizer II, particle clusters, or flocs, were disaggregated into discrete individual grains. By analyzing discrete grains, ambiguity surrounding potential changes in particle packaging during deposition, compaction, sampling and preparation is removed.

2.3 Size Analysis using the Coulter Counter® Multisizer II

2.3.1 Operational Principle

The Coulter Counter Multisizer II can analyze sediments in the size range of 0.5-1000 µm (Milligan and Krank 1991). This analyzer has been reported to exhibit <5 % variability between replicated subsamples (Curran et al. 2004). Less than a 2 % error in the estimation of particle diameters was reported for a similar Coulter instrument (McCave and Jarvis 1973). The basis of the device involves the electrical impedance created by a particle passing through an electric field. A constant current maintained between two electrodes flows through an aperture and becomes impeded when a particle passes through that electric field. As a result, a pulse of differential voltage, proportional to the grain volume, is generated. This change in voltage is used by the instrument to yield a particle diameter via the relationship (McCave et al. 1991):

$$\Delta R = [(8 r_f d) / (3 \pi D^4)] \cdot [1 + 4/5 \, (d/D)^2 + 24/35 \, (d/D)^4 \ldots] \qquad (2.1)$$

where ΔR is the change in resistivity in the electric field between the two electrodes, r_f is the resistivity of the electrolyte solution, d is the particle diameter (µm), and D is the aperture diameter (µm).

The instrument uses a glass tube with an electrode at the top and an aperture and sensing zone at its base. The tube is immersed in a beaker that contains 3 % $NaPO_3$

electrolyte solution, a second electrode and the suspended particles (Fig.2.2). A vacuum at the top of the tube pulls the particles and electrolyte solution through the aperture. As the particles pass through the sensing zone of the aperture, the voltage fluctuation created by each particle is detected and transmitted to the Multisizer processor, where the quantity of individual particles is recorded as well as the calculation of equivalent volumes and diameters (Milligan and Krank 1991). The values of the latter two parameters are derived by approximating the particles to spherical objects and employing the relationship described in Equation 1. Each particle is then assigned an appropriate size class. For this study, the Coulter Multisizer II has 256 channels, or size classes, calibrated to particles of known diameter (Coulter Electronic Inc., 1979).

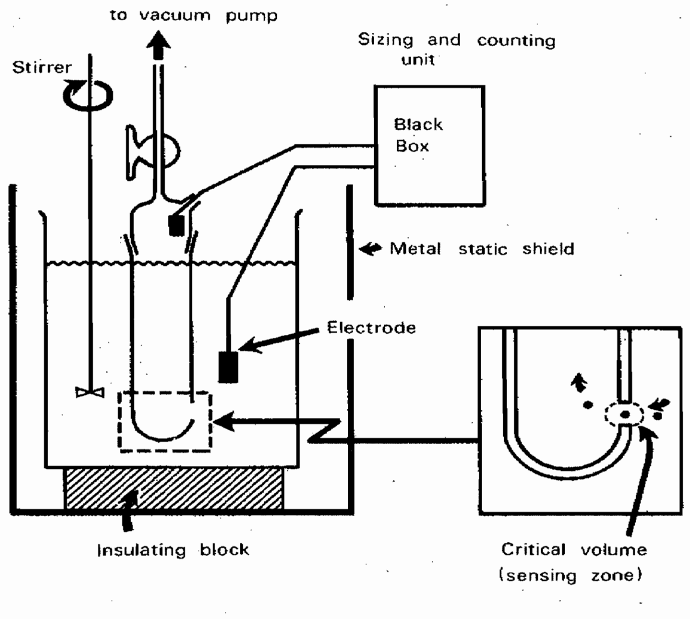

Figure 2.2. Schematic illustration of the main components contained in the Coulter Multisizer II particle size analyzer. Note: The sensing zone is located within the aperture at the base of the tube (From McCave and Syvitski 1991).

Natural sediments typically possess a range of sizes that are too large to characterize with just one tube on the Coulter Counter (Milligan and Kranck 1991). For this study, two aperture sizes (30-µm and 140-µm) were chosen such that the full range of fine silt and clay particle sizes could be measured accurately. These tubes were used for counting and sizing grain diameters of 1 – 12 µm and 8 – 80 µm, respectively. In order to ensure that the apertures were not blocked by particles beyond their sizing capacity, a 25-µm Nitex® screen was used to sieve samples prior to counting with the 30-µm tube. Similarly, a 100-µm screen was used for the 140-µm tube.

After the samples were run through the two specified aperture sizes, the data were plotted by a custom software package, with the logarithm of concentration in p.p.m (parts per million) on the y-axis versus logarithmic grain diameter on the x-axis. The choice to represent the results as log-log frequency plots is based on the idea that sediment size distributions and spectra have a basic exponential nature that is expressed robustly using logarithmic scales (Milligan and Krank 1991). Because two aperture sizes were used, each initial raw data graph contained two distributions (one from each aperture used). An editing function was employed to merge the two distributions into one (Milligan and Krank 1991).

The final step in expressing the results of the disaggregated inorganic grain sizes (DIGS) was to normalize the volumes in each size class via the calculation

$$\text{Normalized Volume } \% = \frac{(V(i))}{\sum_{i=1}^{n} V(i)} \times 100 \qquad (2.2)$$

where V is the volume, i is an index integer with an associated particle diameter (µm), and n is the maximum integer index diameter measured in each sediment sample and typically range from 25 µm to 36 µm (Appendix A) .

2.3.2 Assessment and Treatment of Multiple DIGS Spectra

For DIGS that exhibited irregular shaped spectra due to processing error (e.g. sample too dilute) or spectra that did not exhibit similar characteristics to adjacent spectra within the core, duplicate and triplicate samples were analyzed to ensure quality control. The method for selecting a single optimal spectrum was based on a combination of the following criteria: (1) spectra that contained spikes were discarded in favour of smoother spectra, (2) spectra that contained measurable volume in the most size classes were chosen over spectra with a narrower range of measured size classes and, (3) two spectra that were more similar than a third, in the case of triplicates, were favoured and the criteria listed above were subsequently employed to select a single best distribution plot. To illustrate this process, consider the triplicate runs of DIGS spectra acquired from the core at a depth of 77 cm (Fig. 2.3). Based on the methods delineated above, ‘Run x’ is eliminated based on criteria (1) and (3) while ‘Run y’ is considered unfavourable compared to ‘Run z’ with respect to criterion (2).

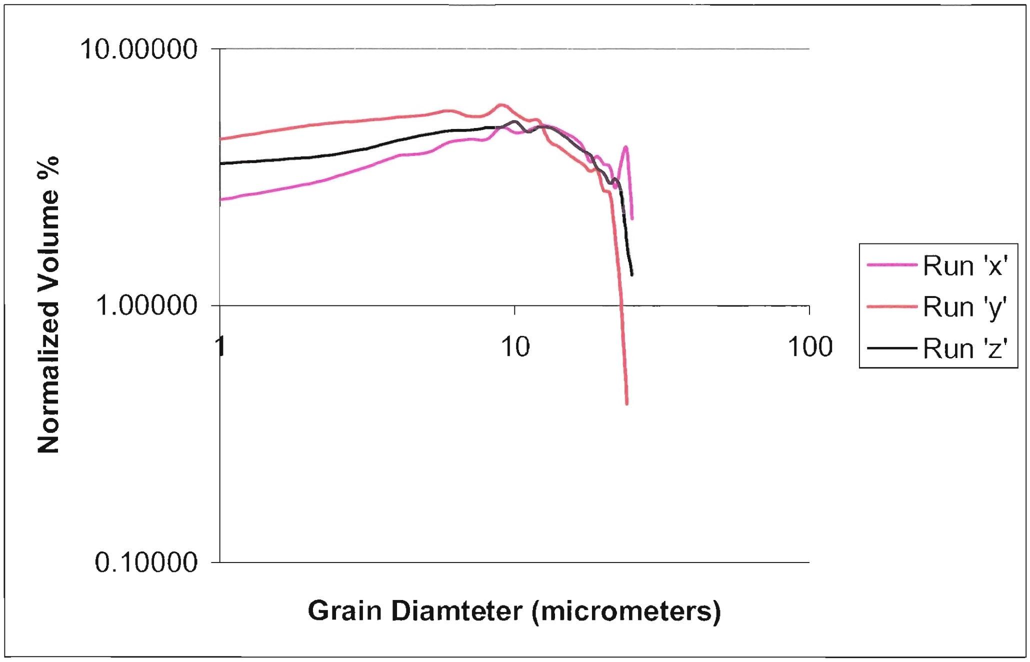

Figure 2.3. Results from three DIGS analyses all corresponding to the same depth in core. See text for criteria concerning the process of selecting the optimal spectrum.

2.4 Parameterizations

The goals of estimating parameters from the bottom sediment DIGS distributions plots were to quantify inherent characteristics of the spectra and to expose possible downcore trends in these characteristics (Appendix B). Describing the size distributions with parameters facilitates both quantitative assessments of data as well as allowing for direct comparison amongst samples.

2.4.1. Sortable Silt Mean Size

The sortable silt mean size parameter is a measure of the mean grain diameter in the size range from 10 μm to 63 μm of the biogenic silicate and siliclastic sediment (McCave et al. 1995; Hall and McCave 2000; Bianchi and McCave 1999). Silt larger than 10 µm presumably can be sorted hydrodynamically, thus recording both spatial and temporal variability of deep-sea current speeds. Smaller sizes are too cohesive for sorting to occur. From the tabulated data set of normalized volumes of each size class, the sortable silt (d_{ss}) diameter in each sample was calculated via the summation function

$$d_{ss} = \frac{\sum_{i=j}^{n} (V(i)d(i))}{\sum_{i=j}^{n} V(i)} \tag{2.3}$$

where $V(i)$ is the normalized volume percent of the size class integer value (i), $d(i)$ is the grain diameter of the size class integer index i (µm), and $d(j)$ equals 10 µm .

2.4.2 Clay-to-Silt Ratio

Clay-to-Silt ratio simply expresses the relative amounts of clay and silt in the range of 1 – 2 µm (Sect. 2.3.1) and >2 – 63 µm, respectively (McCave et al. 1995). The parameter is calculated as

$$\text{Clay-to-Silt Ratio} = \frac{\sum_{i=1}^{k} (V(i))}{\sum_{i=k+1}^{n} (V(i))} \tag{2.4}$$

where k is defined such that $d(k)$ equals 2 µm.

2.4.3 Alternative Parameterization

Kranck et al. (1996) and Curran et al. (2004) established a quantitative relationship that expresses the size distribution of fine sediments in suspension as

$$V(i) = V_o\,(d_i / d_o)^m\ e\text{^}(^{-}(d_i/ \text{đ})^2) \qquad (2.5)$$

where $V(i)$ is the normalized volume percent of size class i, V_o is the normalized volume of the reference diameter d_o (μm), d_i (μm) is the diameter of size class i, m describes the size distribution of the source or parent material with typical values of 0 ± 0.2, and đ (μm), termed 'dhat', is the diameter of the particle grains whose concentration has decreased to 1/e of its initial value in the source distribution. This parameterization is used because it is able to both simplify and adequately describe the size distribution of sediments in suspension (Kranck et al. 1996). It assumes that the size spectrum of the bed sediment mirrors the grain-size distribution of the equivalent suspended sediments in the overlying water column (Kranck et al. 1996). Because this study deals primarily with floc-deposited sediments (Sect. 4.1.1.) this model is an appropriate way to characterize the sediment size and textural characteristics contained in the distribution spectra.

2.4.4 Description of the 'm' and 'đ' variables in the floc-grain-settling model parameter

When terrestrial rocks undergo a combination of chemical and physical weathering, the resulting material is likely to be poorly sorted as well as compositionally heterogeneous. The detrital products of weathering typically follow a power law relationship that produces straight lines when size spectra are plotted using a logarithmic scale (Kranck et al. 1996; Kranck and Milligan 1991). The slope of the fine tail in the sediment distribution plot is parameterized as 'm' (Kranck et al. 1996; Kranck and Milligan 1991). This parameter can be thought of conceptually as typifying the original size distribution of fine particle grains in a given deposit of sediments.

The 'dhat' (đ) variable in the floc-grain-settling model describes the diameter of the particles whose concentration has decreased to 1/e of its value along the line with slope 'm'. Curran et al. (2004) described the 'dhat' parameter as being a suitable indicator of the largest grain size in the distribution. This parameter decreases with distance from the source and with declining energy in the water column (Kranck et al. 1996; Curran et al. 2004).

Figure 2.4 illustrates a typical DIGS spectrum from the core along with a curve generated from the model of Equation 2.5. The agreement between the theoretical and observed size distribution spectra demonstrates both the usefulness and applicability of the model devised by Kranck et al. (1996). The fine tail of the spectrum is characterized by 'm'. In the coarse end of the spectrum, a marked decrease in normalized volume of the larger size classes occurs at diameters near 'dhat'.

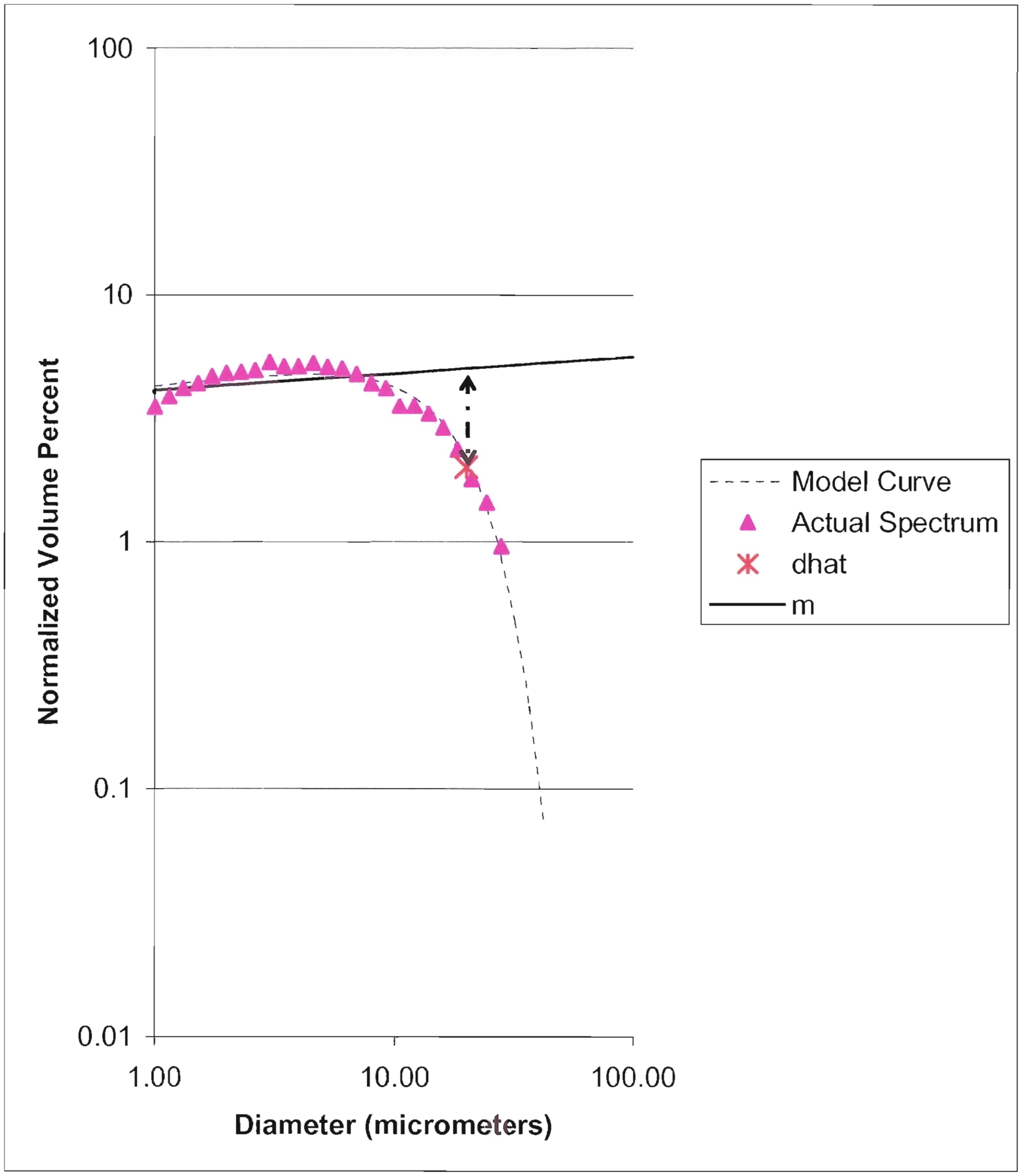

Figure 2.4. Typical log-log DIGS spectra showing a spectrum (pink triangles) from bed sediment sample in core Me-0005-27JC compared to an equivalent curve (dashed blue line) produced from the parameterization of Kranck et al. (1996) and Curran et al. (2004). Dashed double arrow shows the rapid decline in the normalized volume of the coarse fraction towards 'dhat'(asterix). See text for details of parameter variables.

2.5 Chemical And Sedimentological Proxies

Sedimentary deposits on the sea floor are the products of a variety of processes that record and exemplify the dynamics of continents, oceans and water masses from which the materials originated (Futterer 2000; Seibold and Berger 1993). The measurement and analysis of DIGS distribution spectra in this study was primarily aimed at characterizing the nature of the non-carbonate, inorganic fraction of the sediments. Because deep-sea deposits constitute a heterogeneous mixture of material, this study explores, as well, the abundance and flux of biogenous opal for the sampled site[3].

2.5.1 Biogenous Opal

Biogenous opal, a form of amorphous hydrated silicon dioxide ($SiO_2{\cdot}nH_2O$) is the remains of hard parts, or tests, of microscopic marine plankton such as diatoms, silicoflagellates, radiolarians, and sponge spicules. Because opal constitutes a significant fraction of the sediment in this study, it is relevant to briefly describe some of the oceanographic and depositional features associated with its distribution. Seibold and Berger (1993) describe several important factors concerning opal deposition and preservation: (1) Biogenous siliceous deposits are found in areas of upwelling associated with high surface water fertility and primary production, (2) corrosion of silica decreases with increasing depth and surface water fertility, (3) radiolarians and sponge spicules are more likely to be preserved over silico-flagellates and diatoms in the sedimentary record and, (4) the preservation of biogenous opal in the world's ocean is highly contingent on

---

[3] From unpublished data set compiled by Kienast, S.S., Kienast,.M., Francois, R., Mix, A.C., Mollenhhauer G., Eglington, T.I., and S.E. Calvert (2005, *submitted manuscript*)

the amount of opal extraction and deposition within the Antarctic on timescales of tens to hundreds of thousand years.

2.5.2 Mass Accumulation Rate (MAR)

A method used to estimate sediment flux is determining the mass accumulation rate (MAR; given in $g/cm^2/k.y.$) (Francois et al. 2004 and *references* therein), calculated as

$$MAR = LSR \cdot \rho \tag{2.6}$$

where LSR is the linear sedimentation rate (cm/ky), and ρ is the dry bulk density of the sediment (g/cm^3). The age model[4] applied to the LSR in this study is based on Carbon-14 ages *N. dutertrei* and calibrated to calendar years before present (B.P.). For convenience, the ~30 k.y. to present time span of the core is divided into two periods based on the composite oxygen isotope record by Hendy and Kennett (1999) from sediments in the Santa Barbara Basin: (1)Colder sea surface temperatures (SST) are noted for the 30-16 ky B.P interval, which encompasses the Last Glacial Maximum (LGM ~21ky B.P from Ruddiman (2001)) and hereon referred to as glacial periods, (2) the interglacial period, marked by deglaciation (Ruddiman 2001) and warmer SST for the 15 ky to present period, where the 15-10 ky B.P will be referred to as the Transition period into the Holocene (10-0 ky B.P). For the purposes of this study, a linear interpolation was applied between four radiocarbon-dated depths to obtain depth-age equivalences

---

[4] From unpublished data set compiled by Kienast, S.S., Kienast,.M., Francois, R., Mix, A.C., Mollenhhauer G., Eglington, T.I., and S.E. Calvert (2005, *submitted manuscript*)

(assuming 0 cm = 0 ky B.P.). Thus, this core chronology is a best estimate for the studied interval and cannot be considered as yielding exact ages. This cautionary note acknowledges one of the uncertainties regarding age resolution when considering core chronology between closely spaced age horizons described by Francois et al. (2004). Another caveat regarding the MAR method for estimating sediment flux, which this study addresses in more detail, is that it does not distinguish whether the sediment input was vertical or horizontal.

2.5.3 Thorium-230 Isotope vs. MAR Proxy

The production of Thorium-230 (half-life = 75.2 ky) is from the decay of the conservative element Uranium-234 in seawater. Th-230 is insoluble in seawater and is readily adsorbed by settling particles in the water column (Bacon and Anderson 1982). Theoretically, the amount of Thorium-230 scavenged to the seafloor should equal the known amounts produced by the decay of Uranium-234 in the water column for a known time period and is thus useful in estimating the vertical flux of particles to the sea floor (Brown et al. 2002). In practice, observed Thorium concentration in sediments which deviate from the known production rate is accounted for by the sediment redistribution (Paytan et al. 2004). The total vertical flux is calculated as (Bacon and Anderson 1982);

$$^{pr}F_{V}\text{-bulk} = \beta * z / \, xs^{230}Th_{(0)} \qquad (2.7)$$

where β is the production of Th-230 from U decay in the water column (0.0267 dpm m^3y^1), z is water depth (m), and $xs^{230}Th_{(0)}$ is the decay corrected excess of Thorium activity of the sample (dpm/g).

Various authors (Francois et al. 2004; Suman and Bacon 1989) have devised and employed the parameter (ψ), termed the focusing factor, which identifies the ratio between measured MAR and Th-230-based estimates of vertical mass flux where;

$$\Psi = \mathrm{MAR}/\,{}^{pr}F_v\text{-bulk} \tag{2.8}$$

This ratio is assumed to gauge the relative amount of sedimentary material ending up on the seafloor from vertical versus horizontal transport such that focusing factors exceeding 1 imply horizontal addition of sediment to the site. As a result, the focusing factor may serve as a valuable proxy for estimating sediment removal through winnowing or, on the other hand, sediment focusing during a particular interval (Zabel et al. 2000).

Regarding the region of this study, debate concerning the accuracy of Th-230-based vertical flux estimates has arisen[5] (Francois et al. 2004; Paytan et al. 2004; Lyle et al. 2005). Specifically, the latter two papers suggest that sediment focusing is exaggerated by the dissolution of Th-230 in bed sediments. The dissolved Th-230 may leak back into the water column in areas of slowly accumulating surface sediments and then redeposit via particulate scavenging in areas of elevated vertical flux (Lyle et al. 2005). Furthermore, it has been suggested that Th-230 could be preferentially adsorbed

---

[5] Kienast, S.S., Kienast,.M., Francois, R., Mix, A.C., Mollenhhauer G., Eglington, T.I., and S.E. Calvert 2005, *submitted manuscript*

onto particles with high surface areas (Lyle et al. 2005), so its flux may be affected by particle size distribution and packaging in the water column.

CHAPTER 3: RESULTS

3.1 DIGS Results

Disaggregated inorganic grain size (DIGS) distributions exhibit downcore variations through the 200 cm sampled interval. Figure 3.1 shows the results from analyses of 37 depth-correlated samples where individual samples show spectra with size classes ranging from 1 µm to 33±4 µm. The absence of any distinct modes in the distribution spectra characterises these sediments as poorly sorted. The marked decrease in normalized volume percent for size classes greater than 10 µm in the majority of sampled depths identifies these deposits as being predominantly very fine silt to clay.

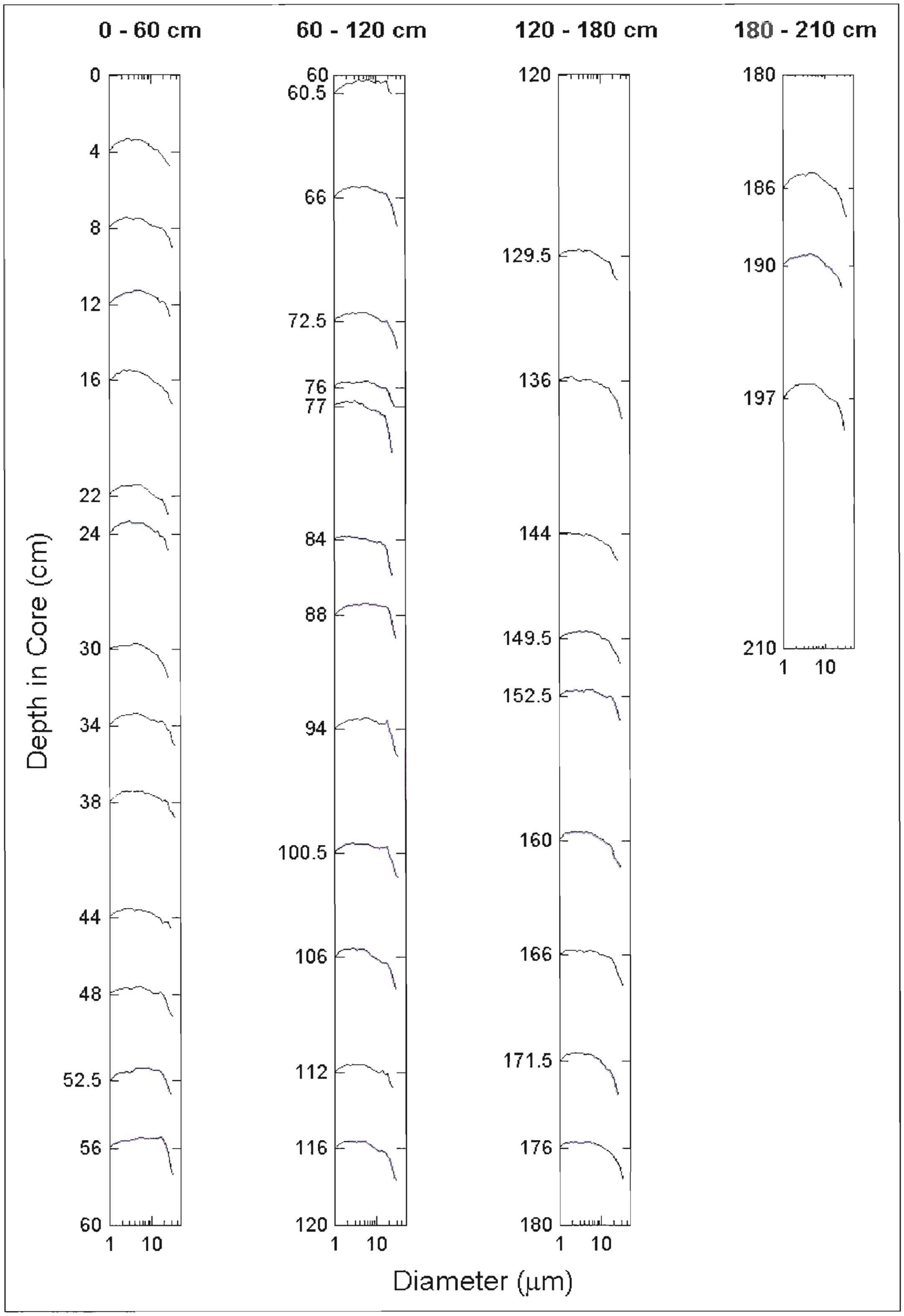

Figure 3.1. DIGS distribution spectra for sampled depths of core ME-0005-27JC

3.2 Results of the Sortable Silt Mean Diameter Parameter

Figure 3.2 shows a plot of mean sortable silt diameter (d_{SS}) with depth in the core. Absolute downcore variations in the sortable silt parameter range in magnitude from 14.5 – 18.8 µm but there is no prominent fining or coarsening trend spanning the entire core interval. For the d_{SS} parameter, excursions are established as a signal when two or more adjacent d_{SS} value plots either above or below the 15.5 - 16.5 µm range. This envelope conservatively represents the magnitude of error associated with estimates of particle diameters (Sect. 2.3.1.). Three notable excursions of sortable silt occur in the core: (1) A minimum at the 84 cm - 77 cm interval, (2) a maximum for the 38 cm - 34 cm interval followed by (3) a sharp decrease at the 30 cm - 22 cm depths.

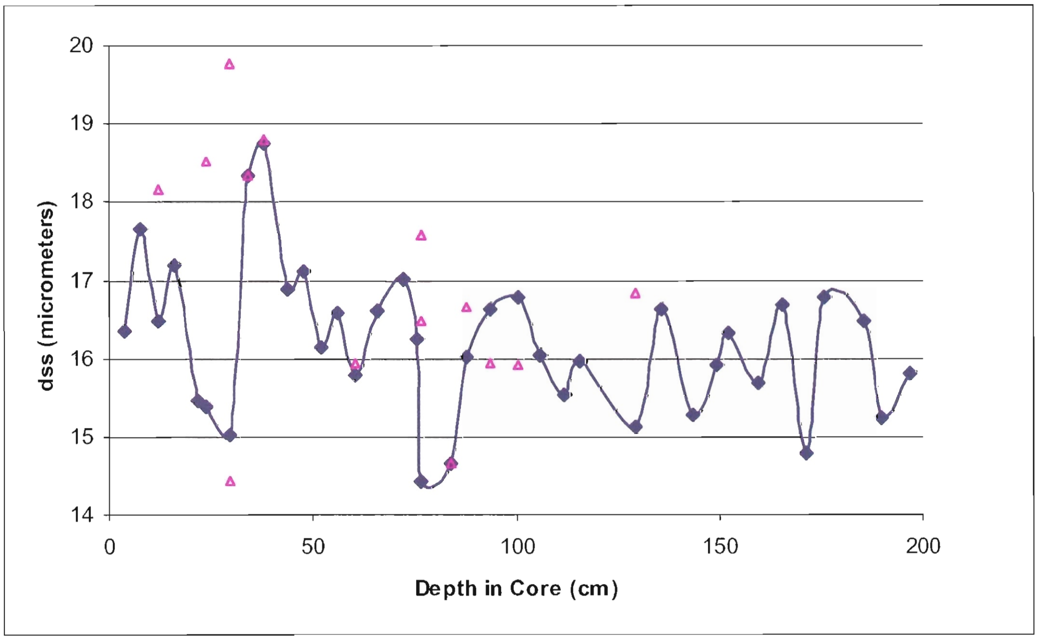

Figure 3.2. Downcore variations in mean diameter of the sortable silt (d_{ss}) population. Connected points show the parameter values; individual open triangles are replicate samples deemed unfavorable by the criteria discussed in 2.2.2 and 2.2.3.

3.3 Results of the Clay-to-Silt Ratio Parameter

Figure 3.3 shows the calculated clay-to-silt ratios for each sampled depth throughout the core interval. Downcore variability of the clay-to-silt parameter ranges from ~0.25 to ~0.46. As these values do not exceed 1, the silt fraction makes up the majority of each sample.

For this parameter, intervals of variability are defined to be those where ratios between two samples vary by >10 % and where an interval contains within it two or more points with high or low values. Increasing ratios occur at the 197 cm - 144 cm and 60.5 cm - 30 cm intervals, and decreasing ratios appear from 136 cm - 88 cm. Between core depths of 60.5 cm - 88 cm a rapid fining (high ratios) is followed by a similarly steep coarsening (low ratios).

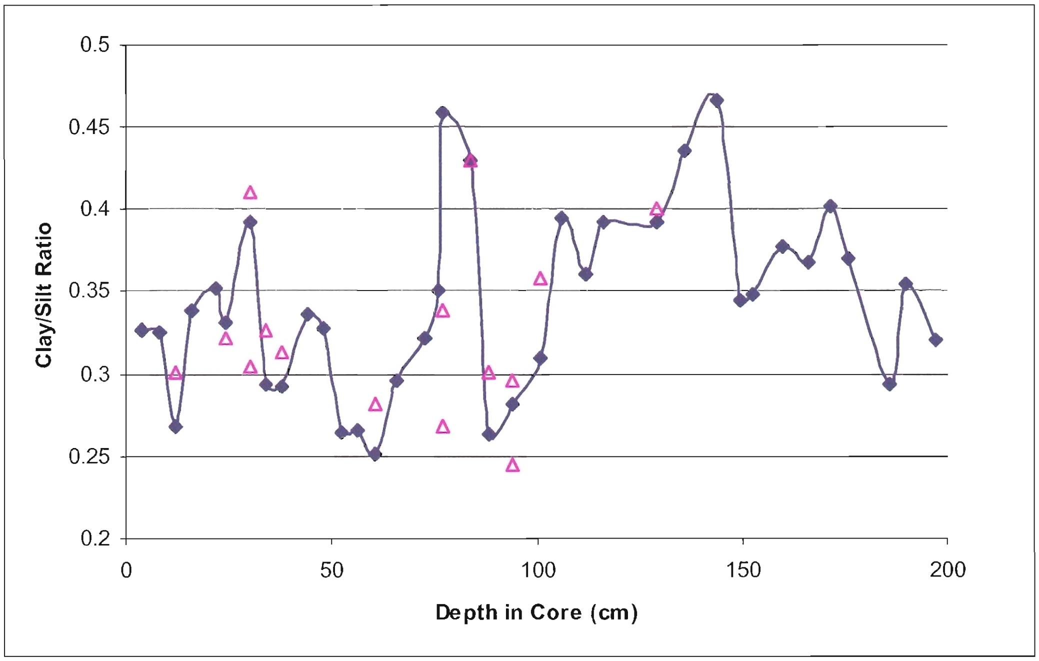

Figure 3.3. Downcore plot of clay-to-silt ratio parameter. Connected points show the parameter values; individual open triangles are replicate samples deemed unfavorable by the criteria discussed in 2.2.2 and 2.2.3.

3.4 Results from Model Parameter 'dhat'

Figure 3.4 illustrates the downcore plot of 'đ'. Throughout the majority of the core interval there are constant values for this parameter, typically in the range of 20±2.5 µm. Excursions for this parameter are similar to those established for the 'sortable silt' parameter, however, the values of 'dhat' have comparatively larger particles with a size range of 17.5 µm to 22.5 µm. Departures from this range are exhibited by a significant rise in the 48 cm – 30 cm interval and a fall in the 94 cm – 76 cm interval.

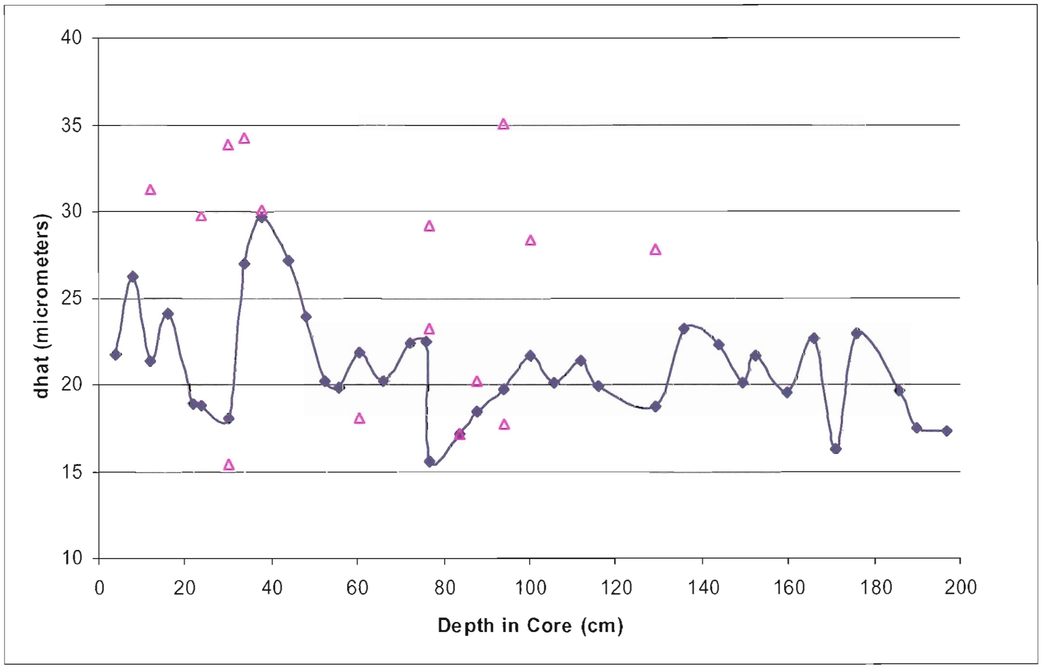

Figure 3.4. Model parameter 'dhat' (đ) plotted downcore. Connected points show the parameter values; individual open triangles are replicate samples deemed unfavorable by the criteria discussed in 2.2.2 and 2.2.3.

3.5 Results for Model Parameter 'm'

The downcore plot of model parameter 'm' (Sect. 2.4.4) exhibits considerable variations in discrete intervals within the core section (Fig. 3.5). Trends and variations are established for this parameter similar to the procedure applied to the clay-to-silt ratios.

Although there is no significant trend from top to bottom, distinctive intervals of variability occur. A decreasing trend in values exists in the 197 cm – 144 cm interval followed by a marked increase to a depth of 88 cm. As well, oscillations in 'm' occur in the 84 cm – 44 cm interval. The relatively stable and consistent values for the uppermost 45 cm section appear to mark a departure from the oscillations characteristic of lower sections in the core interval.

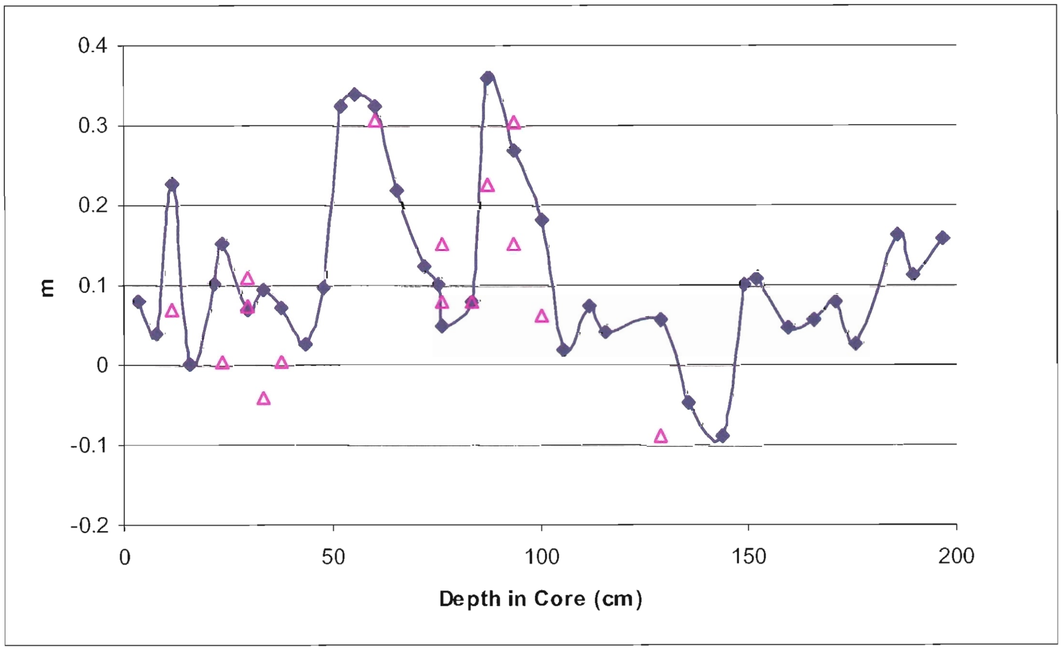

Figure 3.5. Model parameter 'm' plotted downcore. Connected points show the optimal parameter values; individual open triangles are replicate samples deemed unfavorable by the criteria discussed in 2.2.2 and 2.2.3.

CHAPTER 4: DISCUSSION

4.1 Overview

In this chapter, parameters and textural variations are described in further detail with the goal of exploring possible current-related mechanisms to account for the observed changes. Where correlations between textural parameters and chemical data are observed, the nature of the relationship is investigated. As well, this discussion incorporates results from this study into observations and theories made by numerous authors in the literature pertaining to sediment dynamics, paleoclimatology and paleoceanography.

4.1.1 DIGS Spectra

The relatively uniform DIGS distributions throughout the core (Fig. 3.1), indicate that the poorly-sorted sediments are likely the product of floc deposition (Kranck et al. 1996; Kranck and Milligan 1996) and may offer insights into the dominant mode of fine-grained deposition at this site. However, the issue is complicated by two factors: (1) flocs lose their identity upon deposition and become indistinguishable in the bed sediments but can be identified by poorly-sorted fine tails of DIGS spectra (Kranck et al. 1996) and, (2) variations in floc sizes and the extent of their overlap with the sizes of single mineral grains is contingent on depositional regime and benthic conditions (Kurran et al. 2004).

4.1.2 Sediment Texture and Th-230-based Flux Estimates

Based on the interpretation that sediments are floc-deposited and the fact that flocs have relatively low surface area-to-volume ratios, a first order estimate would suggest that the amount of Th-230 would be lowered rather than overestimated (Sect. 2.5.3). However, the assumption cannot be constrained based on the fact that flocs comprise many small constituent grains to which Th-230 could adsorb prior to incorporation of the particles into flocs.

4.2 Sortable Silt and Model Parameter 'đ'

The close correlation between the sortable silt mean diameter (dss) and the 'dhat' parameter through time is demonstrated in Figure 4.1. The similar evolution found in this study agrees with the results from a study of fine-grain sediment dynamics by Curran et al. (2004) on the Laurentian Fan and Sohm Abyssal Plain. Although there are differences in both size and range between the values of these parameters, the coeval fluctuations confirm that they are the product of the same hydrodynamic processes. Because 'dhat' is a proxy for the largest grain size in the sample and 'dss' characterizes an average size of particles greater than or equal to 10 μm, they are inferred to reflect the maximal and average shear-stress during deposition, respectively (Curran et al. 2004).

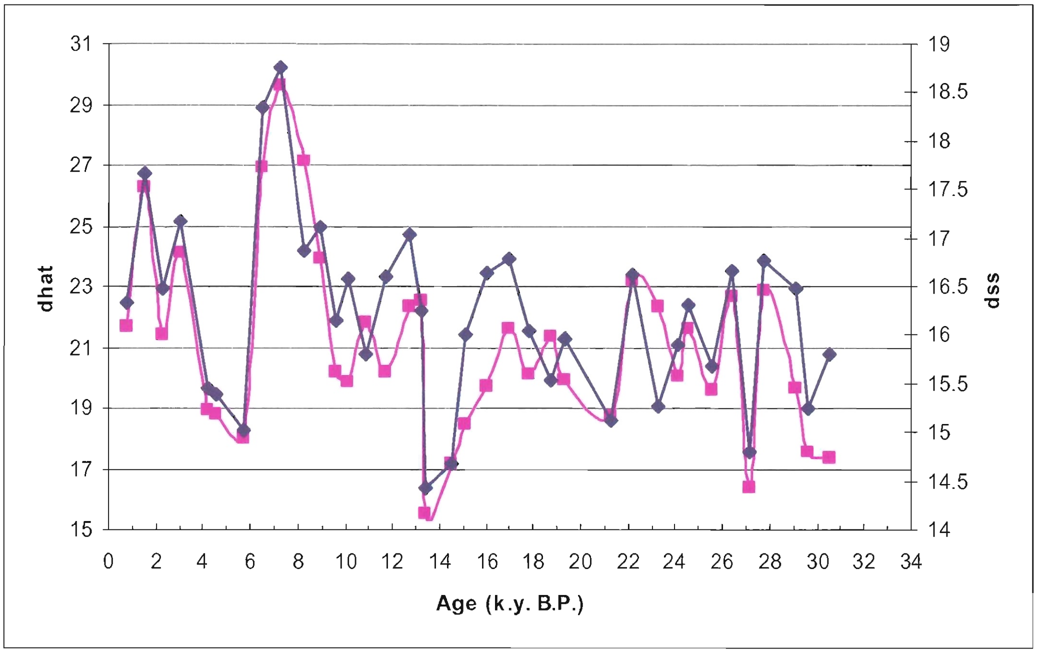

Figure 4.1 Downcore plot of dss (μm) (pink connected squares) and dhat (μm) (blue connected diamonds) vs. age.

4.3 Clay-to-Silt Ratio and Model Parameter 'm'

Figure 4.2 shows how model parameter 'm' evolves with the inverse of the clay-to-silt ratio such that they are almost mirror plots of each other. This relationship is understandable because these two parameters both reflect the relative amounts of fine to coarse material in the sample, albeit from different methods (Sect. 2.4).

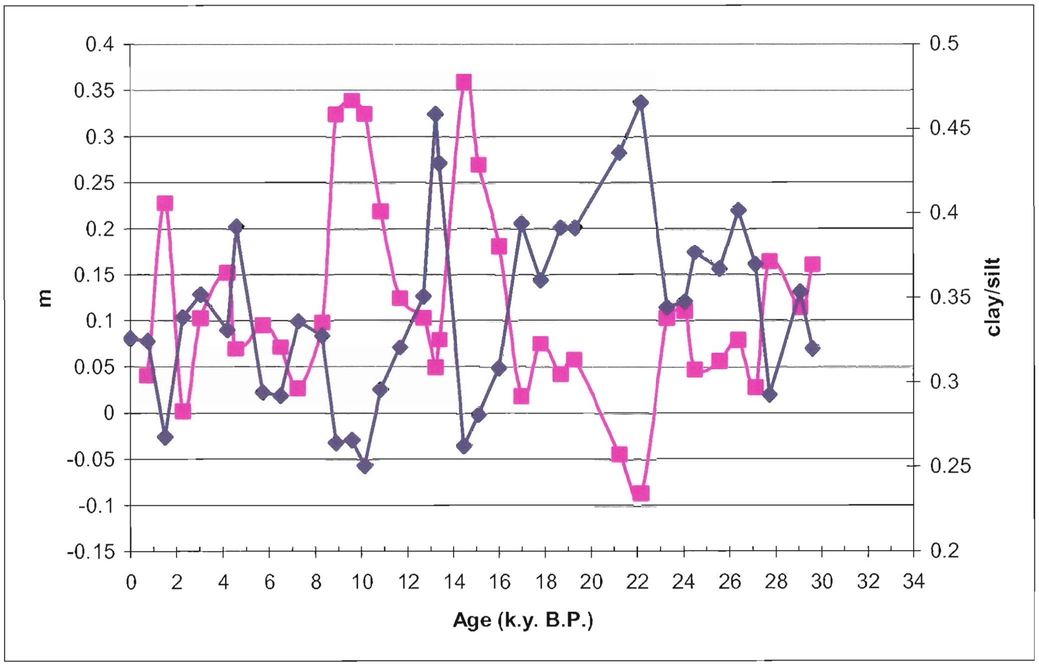

Figure 4.2 Downcore plot of 'm' (pink connected squares) and clay-to-silt ratio (blue connected diamonds) vs. age.

4.4 Paleocurrent Intensity

The sortable silt mean diameter (d_{SS}) may help to reveal variabilities in sediment dynamics for the study site in the EEP. This parameter, devised by McCave et al. (1995), is employed to index relative changes in deep-sea current intensities. Several authors (Hall and McCave (2000); Bianchi and McCave (1999); Hall et al. (2001)) have found that deep water hydrodynamic intensity fluctuates with different climatic intervals. Specifically, warm periods are correlated to faster flow in the bottom currents in the North Atlantic. These authors attribute 4 µm - 6 µm changes in sortable silt diameter, from a population of silt with a range of absolute mean diameters from 10 µm to 20 µm, and changes in clay-to-silt ratios to varying flow conditions. For example, increases and decreases of d_{SS} values sampled from the Iberian Margin were inferred to show faster and slower current speeds, respectively, and were attributed to high frequency climatic oscillations such as the warm Bolling/Allerod and Younger Dryas cold period (Hall and McCave 2000) (Fig. 4.3). Similarly, Holocene fluctuations in deep flow south of Iceland were documented by variability in sortable silt and showed good correlations to warm and cold climates having faster and slower bottom water, respectively, (Fig. 4.7) (Bianchi and McCave 1999). These studies also show systematic decreases in sediment accumulation rates under slower flow conditions. Deep flow patterns in the North Atlantic may not show the same absolute trends as the Pacific Ocean deep water. Indeed, glacial periods in the Pleistocene are thought to be accompanied by faster bottom water currents in the southwestern Pacific with a peak current intensity from ~50 - ~20 ky B.P. (Hall et al. 2001). This period is seen to constrain the overall increasing flow for the past 400 ky, inferred, in part, from high frequency fluctuations in sortable silt diameter with changes recorded by values ranging from 14 µm – 18 µm (Hall et al. 2001). These authors have shown an anti-correlation between the vigor of Pacific and Atlantic deepwater such that faster deep water currents in the Atlantic correspond to slower ones in the Pacific.

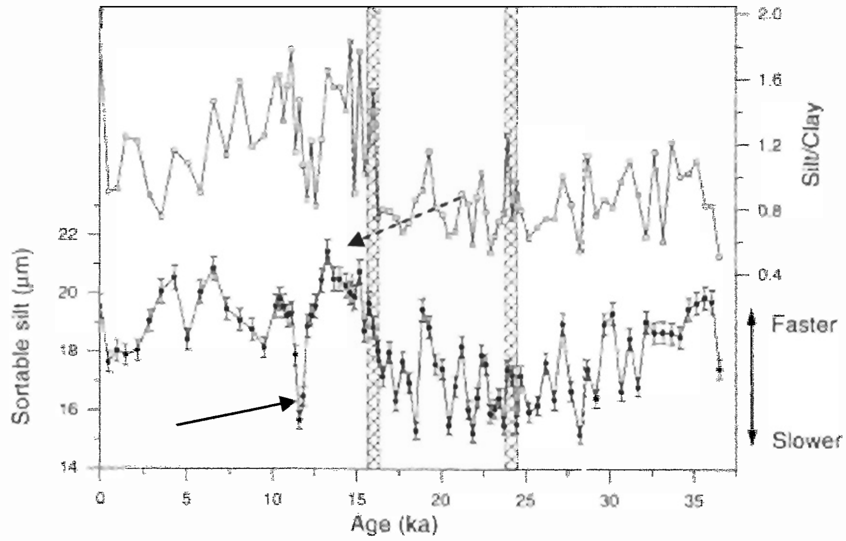

Figure 4.3 Sortable silt (filled circles) and silt-to-clay (empty squares) plotted against age (1ka = one thousand years) for sediments sampled from the Iberian Margin. (After Hall and McCave 2000). Solid and dashed single arrows show the cold Younger Dryas and warm Bolling/Allerod periods, respectively. Note; these authors use silt-to-clay whereas clay-to-silt parameter was employed in this study of the EEP.

Consider the downcore d_{SS} and clay-to-silt parameters from this study plotted against time (Fig. 4.4). From the d_{SS} minima observed in the 4 – 6 ky B.P and 13 - 15 ky B.P intervals, it can be inferred that these intervals represent relative decreases in deep-sea current speeds. This inference may be further substantiated by simultaneous increases in the clay-to-silt ratios. This pattern makes sense because it exemplifies the fact that clay sized particles are deposited from suspension under a slower current regime. Examining the d_{SS} maximum during the 6.5 – 8 ky B.P interval reveals a similar inverse relationship whereby high d_{SS} values correspond to relatively lower clay-to-silt ratios. Indeed, faster flow conditions would suppress deposition of clay-sized particles. The correlations of d_{SS} maxima with clay-to-silt minima, and vice versa, are not exhibited throughout the whole core interval. Apart from the d_{SS} value at ~22.5 ky B.P, however, the inverse correlation generally holds true for the 16 - 31 ky B.P interval.

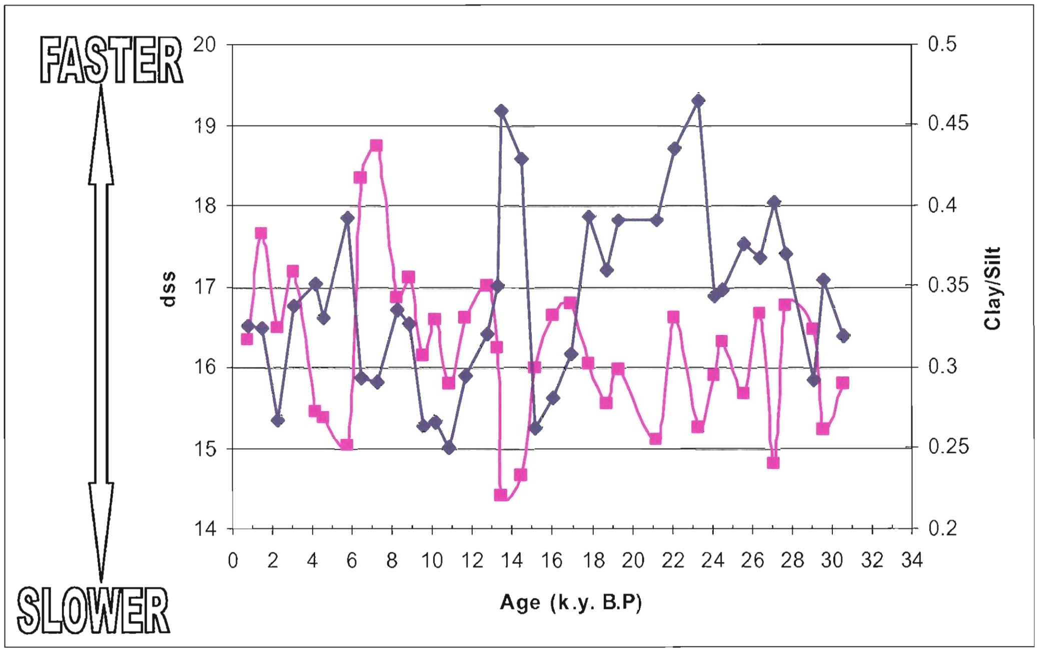

Figure 4.4 Downcore plot of clay-to-silt (blue) ratio and dss (µm) (pink) vs. age. Sidebar arrow demonstrates relative paleocurrent intensity.

One possible explanation for the sortable silt versus clay-to-silt relationship involves a lack of variability in current intensity seen through relatively invariable d_{SS} values. During this interval (16 – 31 ky B.P.), the data suggests that while a relatively stable current speed was maintained, an increase in clay accumulation took place. Increased accumulation may reflect decreased erosion arising from the tendency for clays to be cohesive in bed sediments (McCave et al. 1995; Kranck and Milligan 1991). It may also indicate greater input of clay. Consider the linear sedimentation rates (LSR) and focusing factors (Ψ) for the entire core interval shown in Figure 4.5. Because Ψ maintains values between 1 and 2, sediment focusing via advective inputs is indicated. Focusing is more pronounced, however, in the ~14 – 31 ky B.P interval. This could be the result of the relatively long-term trend of reduced erosion or preferential deposition of clay particles. Comparatively, reduction in the focusing factor from 14 ky to the present, although subtle, suggests shifting hydrodynamic conditions. Decreases in Ψ and LSR coupled with onset of current speed variability indicated by fluctuating d_{SS} values, imply more relative erosion at this site in the ~1 - 13.5 ky B.P interval.

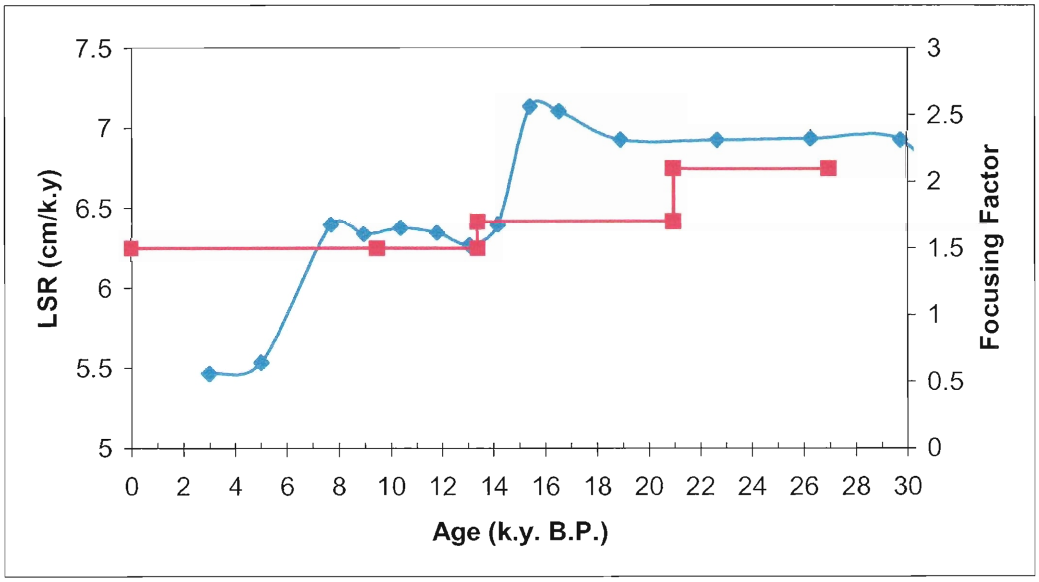

Figure 4.5 Linear sedimentation rate (LSR) (blue) and focusing factor (Ψ) (red) plotted vs. age in core.

McCave et al. (1995) link changes in sediment sorting to energy regimes by suggesting that mean flow conditions, also termed the underlying flow condition, are influenced by mean kinetic energy whereas changes in the variability of the flow conditions are influenced by an added component of eddy kinetic energy (Fig. 4.6). Upcore variations of the sortable silt and 'dha' diameters, which can be visualized as a time series, show three key features: (1) Flow conditions were relatively constant in the 16 - 31 ky B.P interval, (2) the excursion at ~15 ky B.P indicates a change in flow conditions and, (3) the 1 - 13.5 ky B.P interval, characterized by greater current variability.

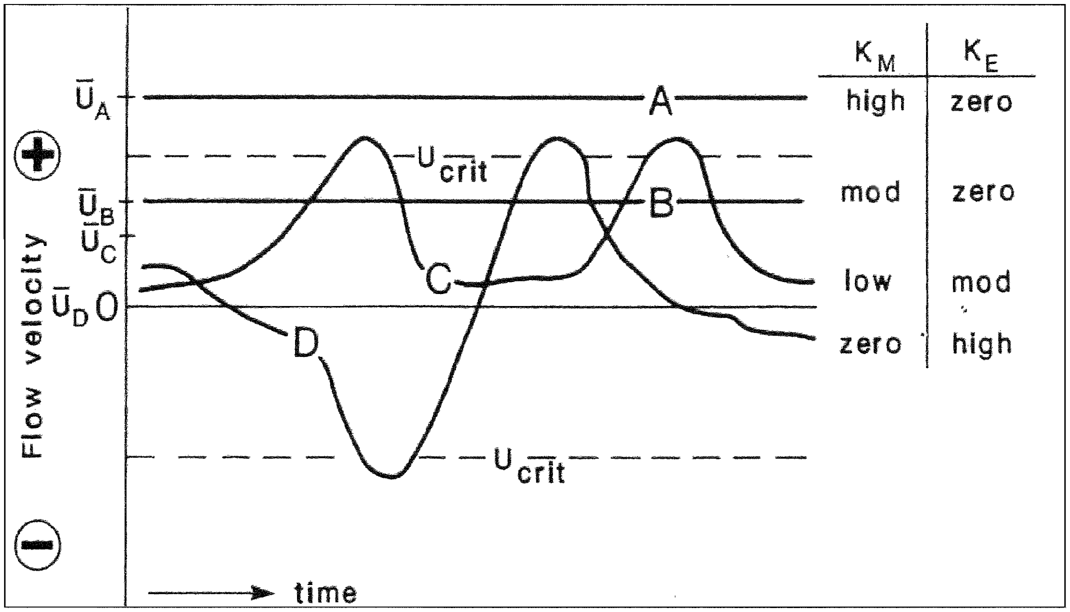

Figure 4.6 Idealized time series of currents. $\bar{U}_{(A\text{-}D)}$ represents different mean flow velocities, U_{crit} is the shear-stress dependent threshold between erosion and deposition of a discrete particle size, K_M and K_E denotes mean kinetic energy and eddy kinetic energy, respectively. Time series "**A**" shows a stable unidirectional current regime with high kinetic energy that is always above critical resulting in constant erosion of material. "**B**" shows a unidirectional stable current regime with moderate kinetic energy incapable of eroding material. "**C**" demonstrates a unidirectional variable current regime that episodically exceeds Ucrit. "**D**" shows a highly variable bidirectional current regime dominated by eddy kinetic energy in the absence of a flow regime containing mean kinetic energy. (From McCave et al. 1995)

Observations and data of modern sedimentological features and hydrodynamics from the north flank of the Carnegie Ridge and Panama Basin (Londsdale and Malfait 1974 and *references therein*) reveal numerous features thought to be related to current strength variability: (1) Bedforms of predominantly foraminiferal sand dunes with amplitude and geometry inferred to have formed under flow conditions of >30 ± 10 cm/sec in a NW transport direction, (2) current meter recording of a maximum flow speed of 13 cm/sec in a general southward direction, (3) colder and denser water mass at 2300 m depth on the southern side of the Carnegie ridge, (4) 15-20 cm/sec abyssal tidal currents superimposed on a 3 cm/sec drift current on the south flank, and (5) large sub-circular depressions thought to have formed from the dissolution of carbonate by highly variable energetic submarine currents (Michaud et al. 2005). Foraminiferal sand dunes may have been formed by episodic spillover of the dense water mass on the southern flank over the ridge saddle into the north Carnegie ridge margin and Panama Basin (Lonsdale and Malfait 1974). Some authors[1] have attributed, in part, very high sediment focusing factors for the northern foot of the Carnegie ridge to these spillovers. These episodic leakage events may have affected the study site documented as this water mass would have to pass over the 2200 m contour and likely entrain some sediments during its migration up the ridge. Such postulated dynamics, in conjunction with the observed rapid abyssal tidal currents on the southern side of the Carnegie Ridge, may offer viable mechanisms for the Holocene/Transition (~1 – 15 ky B.P.) current intensity variations, deduced from the d_{ss} parameter in this study, and increased sediment winnowing exemplified by lower focusing factors.

Several very important questions remain: What was the relative strength of the stable currents characteristic of the 16 – 31 ky B.P glacial interval compared to Holocene/Transition Period (Sect. 2.5.2)? Did the abrupt change at 15 ky B.P mark a real decrease in current intensity, as suggested by the sortable silt parameter, or, rather, do fluctuations observed from this point on mark an interval of transition and a re-equilibration to some new current regime?

Consider, as an example, that the two minima (Fig. 4.4) in the Holocene/Transition characterize an overall slower current regime for this time interval.

---

[1] Kienast, S.S., Kienast,.M., Francois, R., Mix, A.C., Mollenhhauer G., Eglington, T.I., and S.E. Calvert (2005, *submitted manuscript*)

This would imply that the currents prior to 15 ky B.P would have been comparatively stronger. Such an inference agrees with the findings by Hall et al. (2001) of intensified southwest Pacific deep water boundary current (DWBC, ≥2000m water depth) during Pleistocene Glacial periods. This view stems from these authors' interpretation of higher sortable silt values as recording a more vigorous LGM (23– 20 ky B.P) southwest Pacific DWBC as compared to the Holocene/Transition period (13.5 – 0 ky B.P). With respect to the parameters employed in this study, the high frequency oscillation between the minimum and maximum flow intensities at ~5 ky B.P and ~7 ky B.P, respectively (Fig. 4.4), corresponds to opposite flow conditions in the North Atlantic. Specifically, a moderate decrease in flow intensity is seen at 7 ky B.P and a Holocene current intensity peak at 5 ky B.P was observed for deep flow conditions south of Iceland (Fig. 4.7) (Bianchi and McCave 1999). Furthermore, the lowest sortable silt values in this study occur around 14 ky B.P which corresponds to the relative maximum values observed on the Iberian margin in the warm Bolling/Allerod period (Fig. 4.3). As such, the findings in this study are consistent with idea that relative vigor of bottom waters is anti-correlated between the Atlantic and Pacific for the late Quaternary.

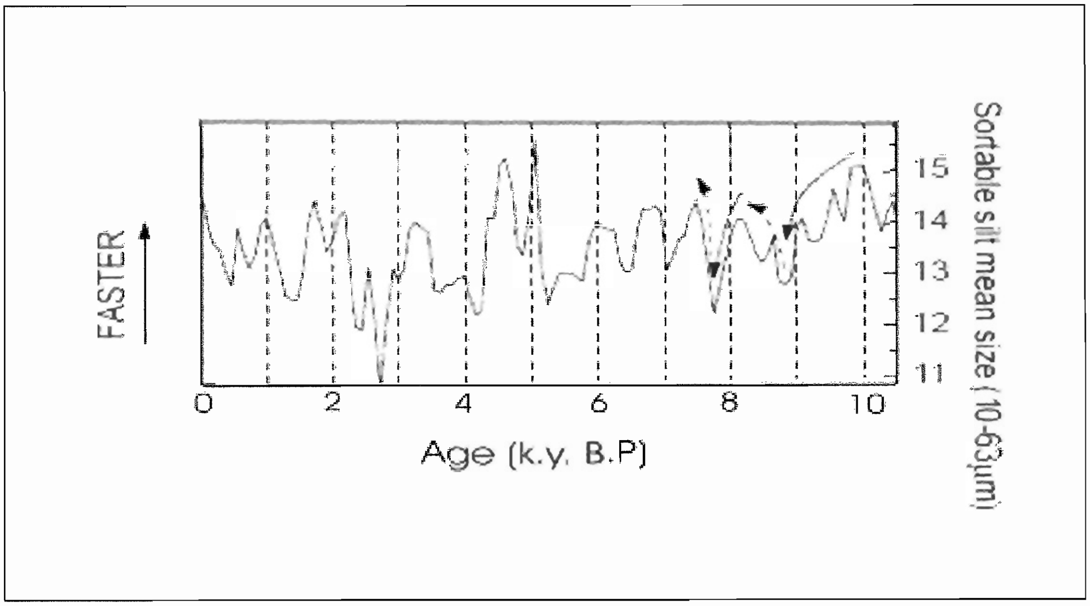

Figure 4.7 Inferred variability in bottom water current intensity south of Iceland during Holocene from the sortable silt parameter (dss). Solid and dashed arrows show trends of decreasing and increasing flow vigor, respectively. (After Bianchi and McCave 1999)

Numerical models for the 20 ky B.P global-ocean tidal kinetic energy show that it was greater and that its dissipation was more focused in the deep ocean during this time (Egbert et al. 2004). It is noted, with caution, that such models do have a considerable margin of error. However, the model provides, to a first order, an approximation of current strength for the 16 – 31 ky B.P interval in this study. With regard to the time series model of McCave et al. (1995), observations of Londsdale and Malfait (1974) for the modern current speeds on the south flank of the Carnegie ridge and the numerical simulation of Egbert et al. (2004), one possible scenario is that the elevated current intensity for the 16 – 31 ky B.P interval was high enough to cause continuous erosion of particles below a certain diameter, similar to time series "A" in Figure 4.6, resulting in a well size-sorted population of grains on the seafloor. This scenario, however, seems unlikely based on a couple of factors: (1) no robust sorting was observed in the DIGS spectra (Fig. 3.1) and , (2) the clay-to-silt ratios (Fig. 4.4) and higher sediment focusing and LSR (Fig. 4.5) in this time period point to a regime of net deposition. A more plausible scenario is that the current regime was not necessarily erosive, thus resembling time series "B", but moderate and stable enough to produce a site of net deposition. A causal mechanism behind this scenario could be the intensified 20 ky B.P abyssal current positioning the deep dense water mass higher up on the Carnegie ridge, thereby establishing, at this site, a relatively fast and stable current regime. Continuing along this line of reasoning, the excursion at ~15 ky B.P could mark a relaxing of abyssal current energy, a subsequent deepening of the dense water mass away from the site, and an introduction of a different, more variable flow regime. The fluctuations of current intensity inferred for the 1 - ~15 ky B.P interval may be the result of the regional episodic intensifications, as postulated by Lonsdale and Malfait (1974), creating a variable regime analogous to time series "C" where such benthic events produce ephemerally erosive conditions.

4.5 Biogenic Silica and Source Distribution Slope "m"

Figure 4.8 shows a plot of percent opal in the inorganic, carbonate-free fraction of the sample along with the calculated values of model parameter 'm' (Eqn. 2.5) versus age. There is a broad through-core correlation between 'm', considered to characterize the size distribution of the unsorted parent distribution from which the bed sediments were derived (Kranck et al. 1996; Kranck and Milligan 1991), and the changes in the percent opal through time. Variability in their relationship does exist, but the strength of the correlation is demonstrated when partitioning the curves into several discrete intervals: First, a gradual decrease in 'm' from 31 - ~23 ky B.P corresponds to a 40% decrease in percent opal over the same interval. Second, a sharp increase in 'm' during the 18 - ~16 ky B.P interval is accompanied by a doubling in percent opal for the same time period, and finally, a rapid decrease in percent opal from ~10 – 7 ky B.P is similarly tracked by a reduction in 'm' values. The most obvious and sustained excursion from this correlation is in the ~1 – 7 ky B.P interval where an increase in opal is accompanied by values of 'm' fluctuating around a constant mean. As well, short-term and less pronounced deviations from the overall through-core trend can be seen in the 22 – 20 ky B.P and 16 – 14 ky B.P intervals. Interestingly, though, is that a similarly short termed interval from 20 - 18 ky B.P, and to a lesser extent even the 15 – 13 ky B.P interval, can be characterized by 'm' and percent opal values that do not exhibit much variation. In general, though, the trends of both 'm' and percent opal appear quite similar for the 31 - 7.5 ky B.P interval.

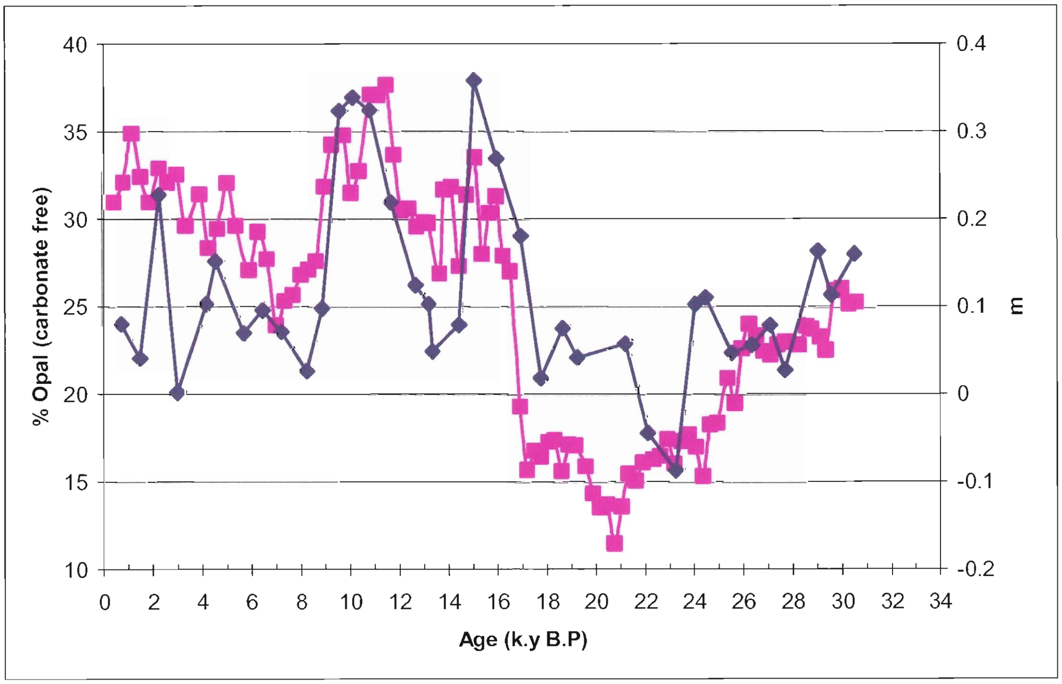

Figure 4.8 Downcore plot of inorganic carbonate free percent opal (pink squares) and model parameter 'm' (blue diamonds) vs. age.

Because variations in ‘m’ document changes in the size distribution of the source material in the sample, it is appropriate to first look to the percent opal values for establishing specifications regarding the type of material being deposited at this site. This is appropriate because the opal fraction in the sediments should presumably have a relatively well-sorted, narrow size range. For simplicity, assume that changes in the opal fraction of the sediments reflect the amount supplied to and buried in the deep ocean. Differences in the opal fraction of the sediment shown in Figure 4.8 demonstrate considerable variation through time. In the context of opal delivery to this site, several trends become apparent: (1) A decrease from ~31 – 21 ky B.P, (2) a rapid increase in the 20 – 16 ky B.P interval followed by some enrichment until 10 ky B.P, (3) some decline from 10 – 7 ky B.P followed by, (4) an increase to ~2 ky B.P.

Consider the time intervals where variations in percent opal and ‘m’ correspondingly track each other. The most robust example of this relationship can be seen in the 18 – 15 ky B.P interval corresponding to 106 cm – 88 cm depths in core, respectively. As such, the latter two depth-correlated samples can serve as fitting end points that adequately constrain the fluctuation during this interval. Figure 4.9 shows the model fit DIGS distribution for these two depths as well as the difference between them.

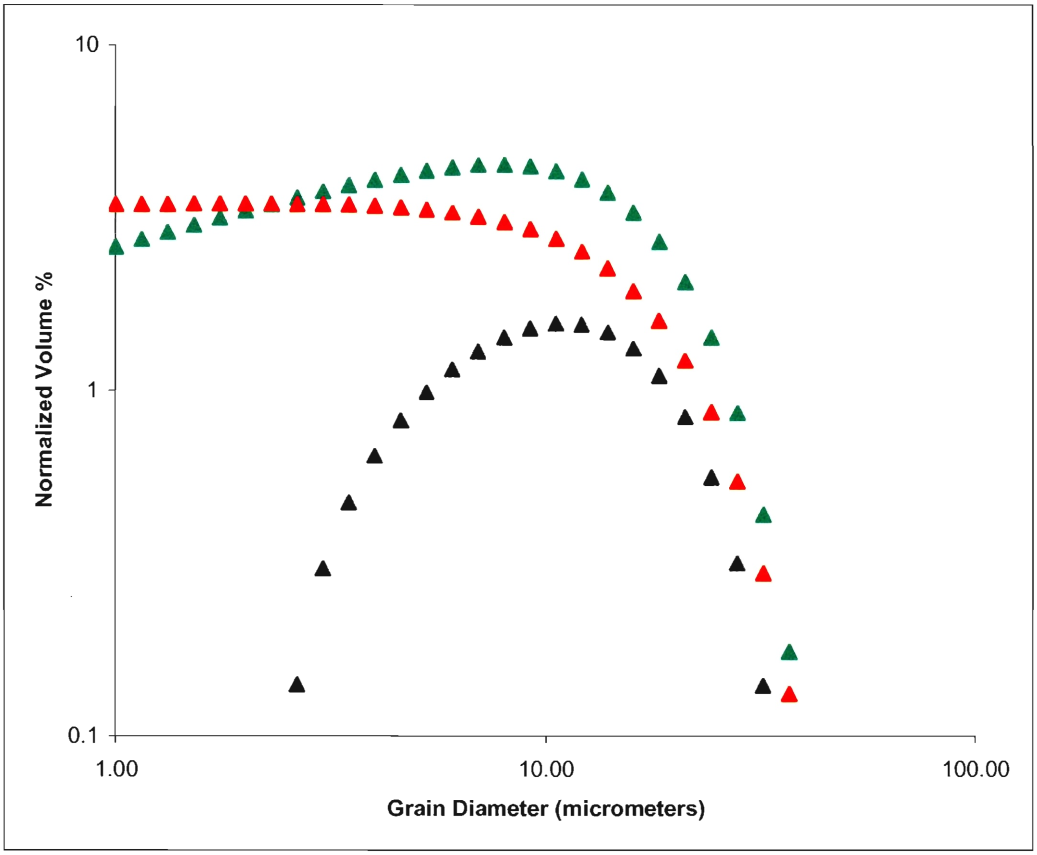

Figure 4.9 DIGS distribution plot for depths 106cm (green) and 88cm (red). The spectrum produced from the difference between them in the >2μm fraction is shown with black triangles.

The variability in 'm' is easily recognized by the differences in the slopes of the fine tails segments of the two DIGS spectra. The difference between them produces a relatively well-sorted distribution with a modal value around 10 μm. Biogenic opal is the frustules, or hard parts, of diatomaceous organisms, and smaller microscopic diatoms has diameters in the range of 5 μm – 20 μm (Seibold and Berger 1993; Brown et al. 2002), so a causal link is proposed. The correlation of 'm' and percent biogenic opal is caused by variable addition of a well-sorted distribution of diatom frustules. This idea agrees with the "size-composition slicing" parameter described by McCave et al. (1995) in determining the proportions and size characteristics of the spectrum. These authors suggest that, in theory, a component subtraction method could be employed to yield the size distribution of carbonate, opal, and terrigenous fraction. It should be cautioned, though, that the structure of opaline frustules is delicate and fragmentation is common in the water column and during burial. Furthermore, sample preparation procedure and handling (Sect. 2.2) could have broken down the opaline tests. A distinction, then, between intact frustules or fragments in the samples cannot be made. It is not within the scope of this study to comment on the compositional or structural state of diatom tests. Rather, in the analysis of grain size and their distribution in and between samples, coarsening of sediments is attributed, in part, to the opal fraction.

Consider the difference between the two size distributions in Figure 4.9 as a function of a compositional change in time. Let the sample at 106 cm equal T_1 and the sample at 88 cm equal T_2. Based on the composition of the sediments in the core described in Section 2.1, the inorganic and calcite free fraction of the samples consists mainly of siliclastic material (L) and biogenic silica (Op). Since we can quantify the change in percent opal, it is worthwhile to perform a simple exercise to explore the covariate 'm' vs. percent opal relationship. To quantify the effect of a changing opal fraction, consider the addition of particles >2 µm between the two depths (Fig. 4.9) in terms of a change in time (T) of the total normalized volume percent (V) occupied by the silt sized particles from $V_1(T_1)$ to $V_2(T_2)$ where;

$$V_1(T_1) = L(T_1) + Op_1(T_1) = 47.09 \qquad (4.1)$$

and

$$V_2(T_2) = L(T_2) + Op_2(T_2) = 64.75 \qquad (4.2)$$

Thus, from T_1 to T_2 there is a 38 % increase in the total volume of silt sized particles. The corresponding increase in percent opal (Op_2 - Op_1) is 87 %. A similar calculation was carried out for sample depths of 56 cm and 34 cm and yielded a 13 % decrease in total volume of silt fraction accompanied by a 19 % decrease in percent opal. Because these numbers are similar to within 1 order of magnitude and, as such, demonstrate a simple quantification of the observed covariate relationship, it is feasible to attribute some of the textural coarsening of the sediment sample to an increase in opal delivery to the site.

Notably, the influence of the opal fraction on the DIGS distribution established in this study is not accurate enough to definitely partition size spectra into terrigenous and opal populations. The relative opal amount in the bulk composition is approximately 15 % and, as such, positioned close to the 10 % composition minimum for obtaining quantitatively precise estimates (McCave et al. 1995). Also, the overlapping sizes between the terrigenous and diatom/sponge spicule fractions make it difficult to distinguish between them. A sizing analysis with "compositional slicing" of bulk (including the dominating carbonate fraction) EEP deep-sea sediments may provide robust results and likely would offer insights into mass accumulation rates, productivity, and lysocline variability.

The correlation between 'm' and percent biogenic opal breaks down for the 7 - ~1 ky B.P interval in the core (Fig. 4.8). One possibility for this departure is that a more gradual correlation may exist, similar to that of the 31 – 21 ky B.P interval, but is not yet resolved in time. This seems unlikely based on a several factors. First, changes in 'm' coeval with changes in percent opal are exhibited on significantly shorter time scales in other parts of the core. Covariations of 'm' and percent opal in the rest of the core have periods of ~2 ky and thus a 6 ky interval should produce, in the least, a loose correlation. Second, excluding the single spike at ~2 ky B.P, the Holocene values of 'm' remain quite stable while opal enrichment takes place. The latter point illustrates, most clearly, the complexity of the decoupling between 'm' and percent opal after 7.5 ky B.P.

If it is accepted that an addition of opal coarsens the sample, logic follows that while enrichment in opal takes place but sediment texture remains the same, then some population of certain grain sizes in the pre-7.5 ky B.P interval must have been removed. As well, an addition of finer grains would produce the same end result. One possibility is that the current intensity, as discussed in the previous sections, played a role in fining the Holocene sediments. This would suggest a relatively slower and stable current regime to produce higher clay-to-silt ratios not observed in the top of the core (Fig. 4.4.). Although the 1-15 ky B.P interval is characterized by a regime with a slower background current, the scenario fails because flow variability during this period is assumed to have caused frequent events of erosion thereby advecting finer material away from the site. So if it is not an issue of hydrodynamic removal, *per se*, then another possibility is that coarser material in the pre-7.5 ky B.P period was not delivered to the site at all. Recall from Section 2.4.3 that 'm' describes the size distribution of the parent material. The dominant modes of delivery for such hemi-pelagic materials to the ocean are either by glacial, fluvial or wind-driven agents of transport (Seibold and Berger 1993). Based on time and latitude, direct delivery of sediments by glaciers to the site is unlikely. Fluvial delivery is viable but is hard to constrain both in time and space when considering the abyssal location and inferred hydrodynamic regime at the core site. Wind transport, however, can move fine material, and can vary on relatively short time-scales (Seibold and Berger 1993). For example, Anderson et al. (2006) delineate several features concerning terrestrially-derived aerosol delivery to the Equatorial Pacific: (1) dust in the sediment samples is compositionally similar to the hemi-pelagic sediments found in the coastal areas off of northern South America, (2) eolian transport of fine lithogenic material to the region has operated continuously, at least, since the LGM (~21 ky B.P) however, (3) fluxes of aerosols to the Equatorial Pacific decreased from the LGM to the Holocene by a range of 0.5 to a factor of 2 (Fig 4.10). Present day records of surface wind patterns off of northern South America show a NWN flow direction (Stuut and Lamy 2004, and references therein) in the general direction of the study site.

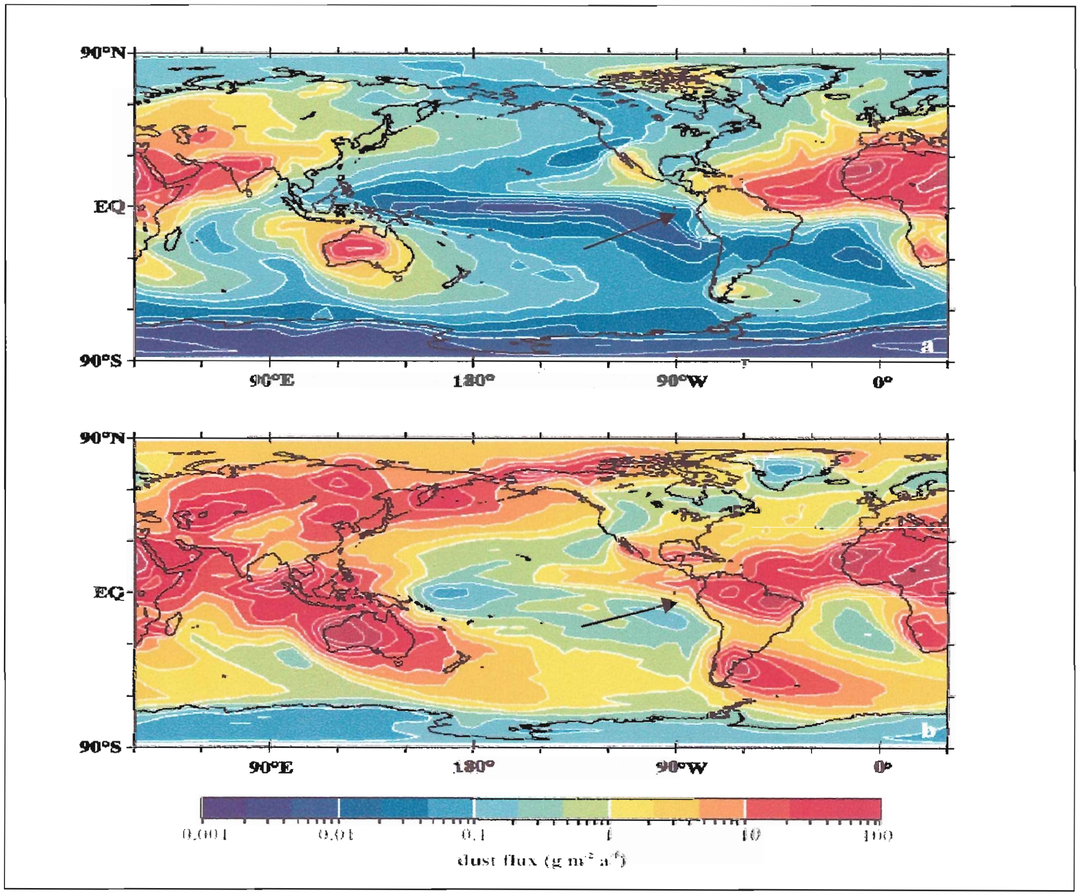

Figure 4.10 Model projections of modern day (a) and LGM (b) global dust fluxes. (After Mahowald et al. 1999). Arrows point the surface waters above the study area.

A typical eolian dust size distribution, extracted from the Chilean continental margin (27° 28' S/71° 15' W), is shown in Figure 4.11. The mode of approximately 29 µm is near the values of 'dhat' for the core. Moreover, when considering that dust (Fig. 4.11) represents a proximal site with respect the source region, it is likely that the distribution would lose some of the coarser material and produce a spectrum with smaller median size with increasing distance away from its source.

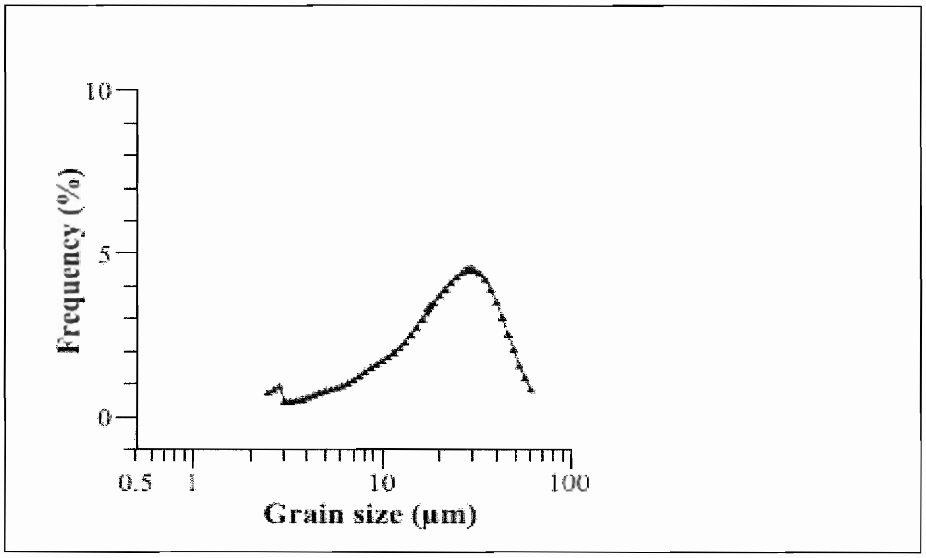

Figure 4.11 End member grain size distribution of fine eolian dust sampled from coastal northern Chile and inferred to have derived from the Atacama Desert. See text for details (Modified after Stuut and Lamy 2004)

Thus, it is possible to add a constraint with regard to the lithogenic components of L from Equations 4.1 and 4.2. For simplicity sake, assume that eolian flux changed in time such that T_1 and T_2 refer to the ~1 - 7.7 ky B.P and 10 - 30 ky B.P intervals, respectively, and there is a doubling in eolian flux from T_1 to T_2 (midpoint of Anderson et al. 2006 estimate). The total terrigenous fraction (L) is now partitioned in two and can be expressed with respect to Op and T(V) as;

$$V_1 (T_1) = L^* (T_1) + 4L_D (T_1) + Op_1(T_1) \tag{4.3}$$

and

$$V_2 (T_2) = L^*(T_2) + 2L_D(T_2) + Op_2(T_2) \tag{4.4}$$

where L* is the aerosol-free terrigenous fraction of the siliclastic sediment. Since it is inferred that the increase between Op_1 and Op_2 ($Op_2 > Op_1$) is offset by the reduction in

L_D during the Holocene, the result is that parameter 'm' stays constant, as observed, and thus $T_1(V_1) \approx T_2(V_2)$.

In summary, the nature of the relationship between 'm' and percent opal through time can be described as follows. The intervals of correlation prior to the Holocene are likely a result variable input of diatom tests . The decoupling between the two variables in the Holocene may be the result of a suppressed delivery of >10 µm silt sized particles to the study site, possibly coincident with a reduction in advected mineral dust during the same time interval. It should be cautioned, though, that there is no clear consensus as to the temporal and spatial variability of mineral aerosols delivery to the oceans (Anderson et al. 2006; Stuut and Lamy 2004; and references therein) during the age limits of this study. Notably, the latter authors argue that aridity has progressively increased since the LGM in northern South America and, as result, suggest a larger vector of mineral aerosol delivery to the oceans in the interglacial and early Holocene periods.

CHAPTER 5: CONCLUSION

5.1 Summary

The study of sediment texture of the siliclastic and biogenic siliceous material in a core from the Eastern Equatorial Pacific has yielded (1) a method for constraining compositional affect on the sediment texture and (2) insights into the hydrodynamic conditions of deposition. Examination of particle size variations was used to reconstruct changes in paleocurrent intensities through time. Specifically, this study used the mean grain size of the silt fraction (>10 µm) in samples to constrain evolving hydrodynamic regimes from the early LGM into the late Holocene. The results show that stable bottom water currents characterizes the 31 ky – 15 ky B.P glacial interval and is reflected by higher sedimentation rates. The paleocurrent reconstruction in this study agrees with other reports related to properties of Pacific deep water showing more vigorous flow during colder periods. From ~15 ky to the present, the flow above the site was variable, with several pronounced fluctuations of sortable silt values. Notably, during the latter Transition/Holocene period, an anti-correlation is observed with respect to the vigor and variability between the North Atlantic and EEP deep water masses This study attributes current intensity changes for the last 30 ky to document dynamic positioning and short-term instability of regional deep water masses.

Analysis of the changes in texture using parameters proposed by Kranck et al. (1996) and refined by Curran et al. (2004) showed how the biogenic component of opal influenced the relative coarseness of the sample. Using this relationship, the influence of changing amounts of siliclastic and biogenic siliceous material on sediment size distribution may be constrained. In the Holocene period, however, addition of biogenic silica did not affect the overall texture in the same way that it did deeper in the core. The decoupling between the opal and coarseness of the sediment may have been caused by a decrease in flux of fine eolian silt to the study site during the Holocene compared to the last glacial period. This hypothesis is consistent with studies that document reduced delivery of aerosols to the Holocene global ocean. In this respect, lack of sediment coarsening accompanied by an increase in percent opal can be accounted for.

5.2 Outlook

Future studies should consider sampling a variety of sites in the EEP. In doing so, correlations could be sought between different locations, offering both spatial and temporal insights into the movement, vigor, and evolution of deep-water masses. Textural analysis of sediments in the EEP is an effective method of indirectly approximating the nature of compositional heterogeneities. As noted in Section 4.5, the use of this method when including the large proportion of calcium carbonate in the samples would likely yield more accurate and constrained descriptions of the size differentiated materials in the bulk sample. Calcite was removed from the samples in this study because the focus was primarily on the siliclastic component of the sediment. However, the study site is significantly shallower than the lysocline and calcium compensation depth in the EEP (Adelseck Jr. and Anderson 1977), so dissolution may not necessarily have such a dominant effect on the calcite fraction of the sediments. Clearly, microscope work could enhance the ground-truthing and accuracy of determining relative proportions of discrete materials. Capturing the size distribution of the entire preserved sediment sample would aid the assessment of hydrodynamic sorting.

There has been a considerable amount of work looking into the mechanisms of opal preservation. Numerous authors have found a positive link between the abundance of dissolved Aluminium from detrital material and enhanced opal preservation in the surface layer of marine sediments (Gallinari et al. 2002; Ridgwell et al. 2002; Dixit et al. 2001; Van Cappellen and Qiu 1997). Such a mechanism would likely influence both the individual mineral constituents and the overall texture of the sediments and should be considered for future studies of EEP sediments. Because biogenic components such as calcite and opal are influenced by the same hydrodynamic conditions as the siliclastic component of sediments, a more complete evaluation of all the constituents and the processes that affect their preservation will only augment our understanding of how bottom water currents influence the texture of deep-sea sediments.

REFERENCES

Adelseck Jr., C.G., and T.F. Anderson. 1977. The late Pleistocene record of productivity fluctuations in the eastern equatorial Pacific Ocean. Geology, **6**: 388-391.

Anderson, R.F., Fleisher, M.Q., and Y. Lao. 2006. Glacial-interglacial variability in the delivery of dust to the central equatorial Pacific Ocean. Earth and Planetary Science Letters, **242**: 406-414.

Bacon, M.P. 1984. Glacial to interglacial changes in carbonate and clay sedimentation in the Atlantic Ocean from Th-230 measurements. Isotope Geoscience, **2**: 97-111.

Bacon, M.P., and R.F. Anderson. 1982. Distribution of thorium isotopes between dissolved and particulate forms in the deep sea. Journal of Geophysical Research, **87**: 2045-2056.

Bianchi, G.G. and I.N McCave. 1999. Holocene periodicity in the North Atlantic climate and deep-ocean flow south of Iceland. Nature, **397**; 515-517.

Brown, J., Colling, A., Park, D., Phillips, J., Rothery, D., and J. Wright. 2002. Ocean chemistry and deep-sea sediments. *Edited* by G. Bearman. Butterworth-Heinemann, Oxford, U.K. pp. 41-42.

Brzezinski, M.A., Pride, C.J., Frank, V.M., Sigman, D.M., Sarmiento, J.L., Matsumoto, K., Gruber, N., Rau, G.H., and K.H. Coale. 2002. A switch from Si(OH) to NO depletion in the glacial Southern Ocean. Geophysical Research Letters. **29**, no. 12; pp.1564-1568.

Coulter Inc. 1979. Coulter Counter model TAII operator's manual. Coulter Electronics Inc., Hialeh, Florida.

Curran, K.J., Hill, P.S., Schell, T.M., Milligan, T.G., and D.J.W. Piper. 2004. Inferring the mass fraction of floc-deposited mud: application to fine-grained turbidites. Sedimentology, **51**: 927-944.

Dixit, S., Van Cappellen, P., and A.J. van Bennekom. 2001. Processes controlling solubility of biogenic silica in pore water buid-up of silicic acid in marine sediments. Marine Chemistry, **73**: 333-352.

Egbert. G.D., Ray, R.D., and B.G. Bills. 2004. Numerical modeling of the global semidiurnal tide in the present day and in the last glacial maximum. Journal of Geophysical Research, **109**: doi: 10.1029/2003JC001973

Francois, R., Frank, M., Rutgers van der Loeff, M.M., and Michael Bacon. 2004. Thorium-230 normalization: An essential tool for interpreting sedimentary fluxes during the late Quaternary. Paleoceanography, **19**: PA1018, doi:10.1029/2003PA000939

Futterer, D.K. 2000. The solid phase of marine sediments. *In* Marine Geochemistry. *Edited* by H.D. Schulz and M. Zabel, Springer-Verlag, Berlin-Heidelberg, pp. 1-22.

Gallinari, M., Ragueneau, O., Corrin, L., DeMaster, D.J., and P. Treguer. 2002. The importance of water column processes on the dissolution properties of biogenic silica in deep-sea sediments I: Solubility. Geochimica and Cosmochimica Acta, **66**: 2701-2717.

Hall, I.R., and McCave, N. 2000. Paleocurrent reconstruction, sediment and thorium focusing on the Iberian Margin over the last 140ka. Earth and Planetary Science Letters, **178**: 151-164.

Hall, I.R., McCave, I.N., Shackleton, N.J., Weedon, G.P., and S. Harris. 2001. Intensified deep Pacific inflow and ventilation in Pleistocene glacial times. Nature, **412**: 809-812

Hendy, I.L. and J.P. Kennett. 1999. Latest Quaternary North Pacific surface-water responses imply atmosphere-driven climate instability. Geology, **27**: 291-294.

Kranck, K. and T.G. Milligan. 1991. Grain size in oceanography. *In* Principles, Methods, and Application of Particle Size Analysis. *Edited* by J.P.M. Syvitski. Cambridge University Press, Cambridge, pp. 332-345.

Kranck, K., Smith, P.C., and T.G. Milligan. 1996. Grain size characteristics of unflocculated sediments I; 'one round' distributions. Sedimentology, **43**: 597-606.

Lonsdale, P and B. Malfait. 1974. Abyssal dune of foraminiferal sand on the Carnegie Ridge. Geological Society of America Bulletin, **85**: 1697-1712.

Loubere, P., Mekik, F., Francois, F., and Sylvain Pichat. 2004. Export fluxes of calcite from the Last Glacial Maximum to present. Paleoceanography, **19**: PA 2018, doi: 10.1029/2003PA000986

Lyle, M., Mitchell, N., Pisias, N., Mix, A., Martinez, J.I., and A. Payton. 2005. Do geochemical estimates of sediment focusing pass the sediment test in the equatorial Pacific?. Paleoceanography, **20**: PA 1005, doi:10.1029/2004PA001019.

Mahowald, N., Kohfeld, K.E., Hansson, M., Balkanski, Y., Harrison, S.P., Prentice, I.C., Shulz, M., and H. Rodhe. 1999. Dust sources and deposition during the Last Glacial Maximum and current climate: A comparison of model results from paleodata from ice cores and marine sediments. Journal of Geophysical Research, **104**: 15895-15916.

McCave, I.N., and J. Jarvis. 1973 Use of the model T Coulter counter in size analysis of fine to coarse sand, Sedimentology, **20**: 305-315.

McCave, I.N. and J.P.M. Syvitski. 1991. Principles and methods of particle size analyses. *In* Principles, Methods, and Application of Particle Size Analysis. *Edited* by J.P.M. Syvitski. Cambridge University Press, Cambridge, pp. 3-22.

McCave, I.N., Manighetti, B., and S.G. Robinson. 1995. Sortable silt and fine sediment size/composition slicing: Parameters for paleocurrent speed and paleoceanography. Paleoceanography, **10**: 593-610.

Milligan,T.G. and K. Kranck. 1991. Electroresistence particle size analyzers. *In* Principles, Methods, and Application of Particle Size Analysis. *Edited* by J.P.M. Syvitski. Cambridge University Press, Cambridge, pp. 109-117.

Mix, A.C., Tiedemann, R., and P. Blum. 2003. Proceedings from ODP, Initial Reports, Leg 202, Site 1238, [online]. Available from http://wwwodp.tamu.edu/publications/202_IR/VOLUME/CHAPTERS/IR202_09.PDF. [cited 2006-09-25] *In* Proceedings of the Ocean Drilling Program Reports.

Michaud, F., Chabert, A., Collot, J.Y., Sallares, V., Flueh, E.R., Charvis, P., Graindorge, D., Gustcher, M.A., and J. Bialas. 2005. Fields of multi-kilometer scale sub-circular depressions in the Carnegie Ridge sedimentary blanket: Effect of underwater carbonate dissolution?. Marine Geology, **216**: 205-219.

Moore, T.C., Heath, G.R., and R.O. Kowsmann. 1973. Biogenic sediments of the Panama Basin. Journal of Geology, **81**: 458-472.

Paytan, A., Lyle, M., Mix, A., and Z. Chase. 2004. Climatically driven changes in oceanic processes throughout the equatorial Pacific. Paleoceanography, **19**: PA 4017, doi: 10.1029/2004PA001024.

Ridgwell, A.J., Watson, A.J., and D.E. Archer. 2002. Modeling the response of the oceanic Si inventory to perturbation, and consequences for atmospheric CO_2. Global Biogeochemical Cycles, **16**: 1071-1097.

Ruddiman, W.F. 2001. Earth's climate: Past and future. W.H. Freeman and Company, New York, pp. 274-351.

Seibold, E. and W.H. Berger. 1993. The Sea Floor: An Introduction to Marine Geology. Springer-Verlag, Berlin-Heidelberg, pp. 121-123.

Sigman, D.M. and E.A. Boyle. 2000. Glacial/Interglacial variations in atmospheric CO_2. Nature, **407**: 859-869.

Smith, B., and D. Sandwell. 1997. Satellite Geodesy: Global topography [online]. Available from http://topex.ucsd.edu/marine_topo/mar_topo.html [cited 21 September 2005]

Stuut, J.B.W. and F. Lamy. 2004. Climate Variability at the southern boundaries of the Namib (southwestern Africa) and Atacama (northern Chile) coastal desertrs during the last 120,000 yr. Quaternary Research, **62**:301-309.

Suman, D.O., and M.P. Bacon. 1989. Variations in Holocene sedimentation in the North American Basin determined from Th-230 measurements. Deep-Sea Research, **36**: 869-878.

Van Cappellen, P. and L. Qiu. 1997. Biogenic silica dissolution in sediments of the Southern Ocean I: Solubility. Deep-Sea Research Part II: Topical Studies in Oceanography, **44**:1109-1128.

Zabel, M., Hensen, C., and M. Schluter. 2000. Back to the ocean cycles: Benthic Fluxes and their distribution patterns. *In* Marine Geochemistry. *Edited* by H.D. Schulz and M. Zabel, Springer-Verlag, Berlin-Heidelberg, pp. 373-395.

Diameter	Depth in Core (cm)									
(µm)	4cm	12cm	16cm	24cm	34cm	38cm	44cm	52.5cm	60.5cm	77cm
1	2.890308	2.61811	3.23918	3.07182	3.22308	2.88216	3.22981	2.65428	2.43454	2.58962
1.15	3.4437	3.02269	3.49393	3.53575	3.77107	3.4335	3.6646	3.05576	2.84123	2.98585
1.32	3.907493	3.35618	4.08543	3.98984	4.00546	3.81333	4.06832	3.44238	3.20334	3.40094
1.52	4.40681	3.74486	4.62537	4.32519	4.30203	4.24997	4.37888	3.69145	3.59331	3.82547
1.74	4.858111	4.0874	4.65104	4.53185	4.58416	4.65968	4.53416	3.9777	3.81616	3.9434
2	5.072315	4.30021	5.20524	4.85468	4.73402	4.77048	4.78261	4.08922	4.17827	4.33962
2.3	5.147827	4.64273	5.55202	4.69199	4.96425	5.09585	4.96894	3.9777	4.26184	4.43868
2.64	5.537744	4.7884	5.23271	4.99475	5.23269	5.11534	4.93789	4.31227	4.31755	4.45283
3.03	5.520612	4.97199	5.55413	4.92982	4.97931	5.14251	4.96894	4.05204	4.40111	4.95283
3.48	5.131474	4.91472	5.28411	4.80877	5.32295	4.96719	4.96894	4.31227	4.65181	4.71226
4	5.438471	5.41273	5.32557	4.79689	4.66462	4.90981	4.59627	4.79554	4.95822	4.81132
4.59	5.472794	5.55967	5.33926	4.91307	4.77586	5.04115	4.7205	5.05576	4.67967	5
5.28	5.347819	5.46227	5.15923	4.84663	4.8188	4.91043	4.78261	5.13011	4.8468	5
6.06	5.158158	5.25824	4.77775	4.62458	4.51634	4.63365	4.53416	5.01859	4.98607	4.85849
6.96	4.809709	4.97906	4.57404	4.50687	4.35384	4.29397	4.34783	5.05576	4.98607	4.65566
8	4.377474	4.54881	4.21145	4.08543	3.97635	3.89811	4.19255	4.94424	4.90251	4.48585
9.19	3.800677	4.24536	3.80288	3.96351	3.61121	3.56226	4.06832	4.86989	4.5961	4.14623
10.56	3.595335	4.08569	3.31279	3.65152	3.37154	3.50563	3.75776	4.42379	4.67967	3.63679
12.13	3.126213	3.88592	3.04943	3.49515	3.16044	3.27828	3.47826	4.60967	4.67967	3.82547
13.93	3.071269	3.7243	2.85402	2.95167	3.16077	2.88102	3.06522	4.42379	4.15042	3.56604
16	2.637377	2.86769	2.48164	2.89641	3.20726	2.97276	2.91615	4.23792	4.67967	3.47642
18.38	2.412104	3.05738	2.40533	2.8748	2.66071	2.86537	2.32298	3.7026	4.90251	2.86792
21.11	1.915645	2.90128	1.9175	2.5449	2.11929	2.3324	2.45031	2.98141	2.81337	3.62264
24.25	1.526124	2.11763	1.73123	2.01421	2.37056	2.22527	2.41615	1.90335	2.46518	4.08491
27.86	1.394437	1.44669	1.14709	1.47215	2.08696	2.13344	1.8323	1.31227	NaN	2.17925
32	NaN	NaN	0.98763	1.48264	2.02642	1.34025	NaN	NaN	NaN	NaN
36.76	NaN	NaN	NaN	1.14511	NaN	1.08619	NaN	NaN	NaN	NaN

Table A.1 Tabulated data showing normalized volumes for 27 separate diameter size classes through various depths in core. Note: “NaN” means “not a number” and refers to the fact that no volume was measured in that size class.

Diameter	Depth in Core (cm)									
(µm)	88cm	100.5cm	106cm	112cm	116cm	129.5cm	149.5cm	160cm	171.5cm	190cm
1	2.62462	3.55095	3.46847	3.51846	3.63727	3.90313	3.51351	3.43534	3.7	3.28084
1.15	3.02008	3.99482	4.03153	3.91072	4.22442	4.30199	3.86486	3.91379	4.225	3.72703
1.32	3.4081	4.32772	4.75225	4.34711	4.66202	4.64387	4.18919	4.61207	4.75	4.27822
1.52	3.66366	4.64213	5.15766	4.648	5.02802	4.92877	4.37838	5	5.125	4.69816
1.74	3.96673	4.80858	5.36036	4.86784	5.27928	5.21368	4.67568	5.08621	5.4	4.93438
2	4.12896	5.01202	5.51802	5.22116	5.31938	5.1567	4.81081	5.34483	5.5	5.24934
2.3	4.39229	4.7531	5.4955	4.94461	5.13384	5.24217	4.86486	5.38793	5.725	5.2231
2.64	4.47364	4.77159	5.63063	5.19043	5.24465	5.35613	4.94595	5.43103	5.675	5.40682
3.03	4.61362	4.64213	5.45045	5.33357	5.10254	5.52707	5.32432	5.34483	5.55	5.69554
3.48	4.67952	4.43869	4.97748	5.11299	4.97106	5.27066	5.10811	5.25862	5.575	5.32808
4	4.60281	4.19826	5.29279	5.29713	5.28825	4.98575	5.10811	5.12931	5.35	5.80052
4.59	4.89295	4.36471	5.33784	5.28188	5.28082	5.09972	5.27027	5.25862	5.4	5.95801
5.28	5.13441	4.23525	5.09009	4.98084	5.16299	5.21368	5.08108	5.17241	5.4	5.82677
6.06	5.06347	4.51267	4.70721	4.59599	4.81145	4.98575	5	4.9569	4.95	5.53806
6.96	4.77767	4.21676	4.34685	4.51761	4.36806	4.58689	4.75676	4.52586	4.625	4.96063
8	4.8066	4.21676	3.87387	4.05303	4.07186	4.18803	4.37838	4.22414	4.275	4.33071
9.19	4.61285	4.14278	3.42342	3.62459	3.65226	3.84615	4.18919	3.79741	3.95	3.88451
10.56	4.51575	3.79138	3.15315	3.4606	3.18156	3.47578	3.54054	3.54741	3.375	3.12336
12.13	4.3888	4.32772	3.04054	3.44506	3.09583	3.33333	3.54054	3.38793	2.95	2.99213
13.93	4.25512	4.03181	2.72523	3.81645	3.18699	2.96296	3.2973	2.87931	2.36	2.86089
16	4.13508	3.86536	2.72523	3.08756	2.79746	2.93447	2.89189	2.5819	2.3725	2.25722
18.38	3.97283	3.68041	2.45495	3.20742	2.41418	2.27635	2.35405	2.36638	1.86	1.96325
21.11	3.25139	3.3845	2.03153	1.95185	2.10789	1.4416	1.78919	1.35776	1.34	1.76115
24.25	1.83964	2.08988	1.34459	1.58511	1.27671	1.16809	1.43784	1.18966	0.67	1.05249
27.86	0.7794	NaN	0.67117	NaN	0.70122	NaN	0.95676	0.84914	NaN	NaN
32	NaN	NaN	NaN	NaN	NaN	NaN	NaN	NaN	NaN	NaN
36.76	NaN	NaN	NaN	NaN	NaN	NaN	NaN	NaN	NaN	NaN

Table A.1. cont'd.

Depth (cm)	Age (k.y B.P.)	dss(μm)	Clay/Silt	'dhat(μm)	‘m'
0	0	N/A	N/A	N/A	N/A
4	0.76	16.338	0.32589	21.7	0.079915
8	1.53	17.658	0.3245	26.257	0.040823
12	2.29	16.488	0.2679	21.409	0.2277
16	3.06	17.181	0.33869	24.113	0.00205
22	4.21	15.451	0.35203	18.93	0.10312
24	4.59	15.39	0.33113	18.782	0.15212
30	5.74	15.03	0.39225	18.039	0.069861
34	6.50	18.338	0.29409	26.946	0.095794
38	7.27	18.744	0.29195	29.628	0.071426
44	8.30	16.875	0.33628	27.161	0.026816
48	8.92	17.119	0.32775	23.916	0.098284
52.5	9.62	16.154	0.2643	20.151	0.32402
56	10.16	16.587	0.26605	19.829	0.33924
60.5	10.86	15.796	0.25097	21.847	0.32477
66	11.71	16.608	0.29561	20.18	0.21963
72.5	12.72	17.024	0.32088	22.357	0.12492
76	13.26	16.246	0.3512	22.516	0.10359
77	13.41	14.432	0.45877	15.555	0.049437
84	14.50	14.668	0.42996	17.149	0.079832
88	15.12	16.005	0.26282	18.45	0.35894
94	16.03	16.642	0.28104	19.706	0.26976
100.5	17.00	16.784	0.30877	21.607	0.18137
106	17.81	16.039	0.39414	20.125	0.018975
112	18.71	15.544	0.36079	21.392	0.075779
116	19.30	15.972	0.3918	19.925	0.042535
129.5	21.25	15.118	0.39152	18.754	0.05818
136	22.18	16.619	0.43613	23.173	-0.04405
144	23.32	15.264	0.46568	22.32	-0.08634
149.5	24.10	15.907	0.34445	20.049	0.10316
152.5	24.53	16.316	0.34792	21.65	0.11073
160	25.60	15.674	0.37706	19.564	0.04758
166	26.41	16.671	0.36734	22.702	0.056665
171.5	27.15	14.804	0.40195	16.363	0.079419
176	27.75	16.773	0.36998	22.897	0.028231
186	29.09	16.471	0.29312	19.659	0.16441
190	29.63	15.242	0.3538	17.554	0.11469
197	30.57	15.803	0.32033	17.376	0.16107

Table B.1 Age-depth correlated parameter values. Note: A linear interpolation was performed between the following anchor pts. ((depth (cm) = age (k.y B.P.)): (41 = 7.84; 91 = 15.58; 120 = 17.2; 160 = 25.6).